The Astrophysical Journal, 917:3 (26pp), 2021 August 10 https://doi.org/10.3847/1538-4357/abff51

Excitation of Polycyclic Aromatic Hydrocarbon Emission: Dependence on Size Distribution, Ionization, and Starlight Spectrum and Intensity

B. T. Draine[1], Aigen Li[2], Brandon S. Hensley[1,6], L. K. Hunt[3], K. Sandstrom[4], and J.-D. T. Smith[5]
[1] Dept. of Astrophysical Sciences, Princeton University, Princeton, NJ 08544, USA; draine@astro.princeton.edu
[2] Dept. of Physics and Astronomy, University of Missouri, Columbia, MO 62511, USA
[3] INAF—Osservatorio Astrofisico di Arcetri, Largo E. Fermi 5, I-50125 Firenze, Italy
[4] Center for Astrophysics and Space Sciences, University of California, 9500 Gilman Drive, San Diego CA 92093, USA
[5] Dept. of Physics and Astronomy, University of Toledo, Toledo, OH 43606, USA
Received 2020 November 12; revised 2021 May 6; accepted 2021 May 6; published 2021 August 6

Abstract

Using physical models, we study the sensitivity of polycyclic aromatic hydrocarbon (PAH) emission spectra to the character of the illuminating starlight, to the PAH size distribution, and to the PAH charge distribution. The starlight models considered range from the emission from a 3 Myr old starburst, rich in far-ultraviolet (FUV) radiation, to the FUV-poor spectrum of the very old population of the M31 bulge. A wide range of starlight intensities is considered. The effects of reddening in dusty clouds are investigated for different starlight spectra. For a fixed PAH abundance parameter $q_{\rm PAH}$ (the fraction of the total dust mass in PAHs with $<10^3$ C atoms), the fraction of the infrared power appearing in the PAH emission features can vary by a factor of two as the starlight spectrum varies from FUV-poor (M31 bulge) to FUV-rich (young starburst). We show how $q_{\rm PAH}$ can be measured from the strength of the 7.7 μm emission. The fractional power in the 17 μm feature can be suppressed by high starlight intensities.

Unified Astronomy Thesaurus concepts: Interstellar dust (836); Interstellar emissions (840); Dust continuum emission (412)

1. Introduction

Strong infrared (IR) emission features at 3.3, 6.2, 7.7, 8.6, 11.2, 12.7, and 17.1 μm are prominent in the spectra of normal star-forming galaxies (see the review by Li 2020), and these emission features have been observed in the spectra of galaxies at redshifts $z > 4$ (Riechers et al. 2014; Armus et al. 2020). Leger & Puget (1984) and Allamandola et al. (1985) proposed that these features are radiated by the vibrational modes of polycyclic aromatic hydrocarbon (PAH) molecules, and this hypothesis is now generally accepted (Tielens 2008; Li 2020).

Except for regions with high-pressure hot plasma—which are thought to contribute negligibly to PAH emission from galaxies—excitation of PAHs is dominated by absorption of starlight photons. The photon absorption produces electronic excitation of the PAH, usually followed by rapid "internal conversion" of the electronic excitation into vibrational energy. The vibrationally excited nanoparticle then cools by infrared emission. If ergodicity is assumed, a realistic vibrational density of states (to relate the vibrational energy to temperature) and assumed infrared band strengths then allow one to calculate the time-averaged emission spectrum for PAHs heated by starlight photons.

The emission spectrum of a galaxy, or of a region within a galaxy, must depend not only on the abundance and composition of the PAH population, but also on the spectrum of the starlight responsible for exciting the PAHs. For example, the PAH emission spectra in M31 are seen to vary from the central bulge to the star-forming rings (Hemachandra et al. 2015). Most previous modeling of PAH excitation (e.g., Li & Draine 2001; Draine & Li 2007) assumed a standard starlight spectrum estimated for the diffuse starlight at the location of the Sun, with only a few explorations of other illuminating spectra (e.g., Li & Draine 2002; Galliano et al. 2008; Draine 2011a; Mori et al. 2012; Draine et al. 2014).

The aim of the present paper is to calculate the PAH emission for a range of starlight spectra and intensities appropriate in different environments, to provide model results that may be useful in interpretation of existing PAH emission spectra measured by ISO, Spitzer, and AKARI, or by future facilities such as James Webb Space Telescope (JWST). For the adopted physical model of PAHs, we seek to delineate the sensitivity of PAH emission spectra to variations in the spectrum of the starlight that is heating the PAHs.

In addition to using the local diffuse starlight spectrum (which continues to be a good proxy for the overall radiation in star-forming galaxies), we also consider extreme examples, ranging from the integrated light from a very young starburst population, to the light from a very old evolved stellar population. We investigate the effects of reddening of the starlight by dust. We also examine the sensitivity of the model emission spectra to possible changes in the size distribution of the PAHs, as well as their degree of ionization.

The paper is organized as follows: Section 2 describes and characterizes the starlight spectra that are employed. Section 3 describes the calculational approach, with examples of temperature distributions shown in Section 4, and time-averaged emission spectra for individual PAHs presented in Section 5. The adopted PAH size distribution, and the emission spectra for such PAH mixtures, are presented and discussed in Section 6. The effect of varying the PAH ionized fraction is examined in Section 7, and the sensitivity to the PAH size distribution is investigated in Section 8. The dependence of the $F(11.2\ \mu{\rm m})/F(7.7\ \mu{\rm m})$, $F(6.2\ \mu{\rm m})/F(7.7\ \mu{\rm m})$, $F(3.3\ \mu{\rm m})/F(7.7\ \mu{\rm m})$, $F(3.3\ \mu{\rm m})/F(11.2\ \mu{\rm m})$, and $F(17\ \mu{\rm m})/F(11.2\ \mu{\rm m})$ band ratios on the starlight spectrum, intensity, PAH size

[6] Spitzer Fellow.

distribution, and PAH ionization are evaluated and discussed in Section 9, and summarized in Section 10.

2. Radiation Fields

2.1. Unreddened

We consider starlight from various stellar populations. We include unreddened spectra from the single-age stellar population ("starburst") models of Bruzual & Charlot (2003, hereafter BC03) for ages t ranging from 3 Myr to 1 Gyr. The BC03 models assume the stars to form with a standard initial mass function from gas with heavy-element mass fraction $Z = 0.02$ (i.e., near-solar metallicity). We also include one very low-metallicity model with $Z = 0.0004 \approx 0.02\,Z_\odot$ and $t = 10$ Myr to examine the effect of varying Z.

We also consider the "BPASS" single-age stellar population models (Eldridge et al. 2017; Stanway & Eldridge 2018), which include the effects of binary stars. We consider the same range of ages as for the BC03 models, and include one BPASS low-metallicity example (for $t = 10$ Myr, with $Z = 0.001 \approx 0.05\,Z_\odot$).

In addition to the BC03 and BPASS models, we consider the solar neighborhood spectrum as representative of the typical interstellar radiation field in the diffuse interstellar medium (ISM) of a star-forming galaxy with more-or-less steady star formation for the past $\sim$10 Gyr, with the starlight reddened by distributed interstellar dust. We use the model of Mathis et al. (1983; hereafter MMP) for the starlight in the solar neighborhood, but with slightly modified parameters (see discussion in Draine 2011b): the dilution factor for the 3000 K component is increased from $W = 4 \times 10^{-13}$ to 7×10^{-13}, and the dilution factor for the 4000 K component is increased from $W = 1.0 \times 10^{-13}$ to 1.65×10^{-13}. We refer to this as the modified MMP (mMMP) starlight spectrum, with energy density per unit frequency $u_{\rm mMMP,\nu}$, and total starlight energy density

$$u_{\rm mMMP} = 1.043 \times 10^{-12}\ {\rm erg\ cm^{-3}}. \quad (1)$$

We also consider starlight from a very old stellar population, using the spectrum of stars in the bulge population of M31 adopted by Groves et al. (2012). The M31 bulge spectrum may be representative of the starlight heating dust in an elliptical galaxy.

Because we are considering the heating of dust grains in regions where the hydrogen is predominantly H I or H_2, the starlight spectra in all cases are cut off at the Lyman limit, $h\nu = I_{\rm H} = 13.6$ eV.

The starlight intensity will be characterized by the heating effect on the grains that dominate the far-infrared (FIR) emission. We calculate the rate of energy absorption by a specified "standard grain." For the standard grain, we adopt a 1.6:1 oblate "astrodust" grain (Draine & Hensley 2021), with porosity $\mathcal{P} = 0.2$ and effective radius $a_{\rm eff} = 0.1\,\mu$m. Let $C_{\rm abs}^{\rm (Ad)}(\nu)$ be the orientation-averaged absorption cross section for this standard grain, c the speed of light, and $u_{\star,\nu}$ the starlight energy density per unit frequency. The standard mMMP radiation field produces a heating rate

$$h_{\rm ref} \equiv \int d\nu\ u_{\rm mMMP,\nu}\ c\ C_{\rm abs}^{\rm (Ad)}(\nu) = 1.958 \times 10^{-12}\ {\rm erg\ s^{-1}} \quad (2)$$

for our standard astrodust grain ($a_{\rm eff} = 0.1\,\mu$m, $b/a = 1.6$, $\mathcal{P} = 0.2$).

For each spectral shape $u_{\star,\nu}$ we define a dimensionless parameter

$$\gamma_\star \equiv \frac{\left[\int d\nu\ u_{\star,\nu}\ C_{\rm abs}^{\rm (Ad)}(\nu)\right] \Big/ \left[\int d\nu\ u_{\star,\nu}\right]}{\left[\int d\nu\ u_{\rm mMMP,\nu}\ C_{\rm abs}^{\rm (Ad)}(\nu)\right] \Big/ \left[\int d\nu\ u_{\rm mMMP,\nu}\right]}. \quad (3)$$

$\gamma_\star$ is the spectrum-averaged absorption cross section for the standard grain relative to the spectrum-averaged absorption cross section for the mMMP starlight spectrum. $\gamma_\star$ is a measure of how effective a given radiation spectrum is (relative to the mMMP spectrum) for heating "standard" dust. By definition, $\gamma_\star = 1$ for the mMMP spectrum; $\gamma_\star > 1$ for bluer starlight (more readily absorbed by dust), and $\gamma_\star < 1$ for redder starlight (less effective for dust heating).

For each spectral shape, we define a reference energy density

$$u_{{\rm ref},\star} \equiv \frac{u_{\rm mMMP}}{\gamma_\star} \quad (4)$$

that produces the standard amount of heating ($h = h_{\rm ref}$) for our standard grain. The intensity of radiation heating the dust in a region can be estimated from the wavelength of the FIR emission peak, which depends on the temperature (and therefore the heating rate) of the $\sim$0.1 μm grains that dominate the FIR emission. We characterize the heating effect of a radiation field $u_{\star,\nu}$ by a dimensionless intensity parameter

$$U \equiv \frac{\int d\nu\ u_{\star,\nu}\ c\ C_{\rm abs}^{\rm (Ad)}(\nu)}{h_{\rm ref}} = \frac{u_\star}{u_{{\rm ref},\star}} = \gamma_\star \frac{u_\star}{u_{\rm mMMP}} \quad (5)$$

where $u_\star$ is the energy density of the radiation. With the definition in Equation (5), radiation fields with different spectra but the same U will heat the standard grain to the same temperature, resulting in the same FIR emission spectrum.

The "hardness" of the starlight is indicated by the mean energy per absorbed photon for a grain X,

$$\langle h\nu \rangle_{\rm abs}^{\rm (X)} \equiv \frac{\int d\nu\ u_{\star,\nu}\ h\nu\ C_{\rm abs}^{\rm (X)}(\nu)}{\int d\nu\ u_{\star,\nu}\ C_{\rm abs}^{\rm (X)}(\nu)}. \quad (6)$$

Table 1 gives $\langle h\nu \rangle_{\rm abs}$ for our standard astrodust grain, and also for a PAH cation. As expected, the harder radiation fields (e.g., the 3 Myr old starburst) have larger $\langle h\nu \rangle_{\rm abs}^{\rm (Ad)}$. Because the opacity of the PAH nanoparticles rises more rapidly in the UV, $\langle h\nu \rangle_{\rm abs}^{\rm (PAH)}$ can be significantly larger than $\langle h\nu \rangle_{\rm abs}^{\rm (Ad)}$ when the radiation field is dominated by starlight from cool stars, as for the M31 bulge.

The starlight spectra, all scaled to give the same $U = 1$ heating rate for our standard astrodust grain, are shown in Figure 1. Because the $t = 10$ Myr $Z = 0.0004$ and $t = 3$ Myr $Z = 0.02$ starburst spectra are very similar for $h\nu < 13.6$ eV (see Figure 1(a)), results calculated below for the $t = 3$ Myr $Z = 0.02$ spectrum may be taken to apply to the $t = 10$ Myr $Z = 0.0004$ case.

2.2. Reddened Starlight

In addition to studying the heating for the above-described starlight spectra, we also consider the case of starlight incident on dust clouds, with the radiation field within the cloud attenuated and reddened by intervening dust. As a representative case, we consider dust clouds with extinction $A_V \approx 2$ mag.

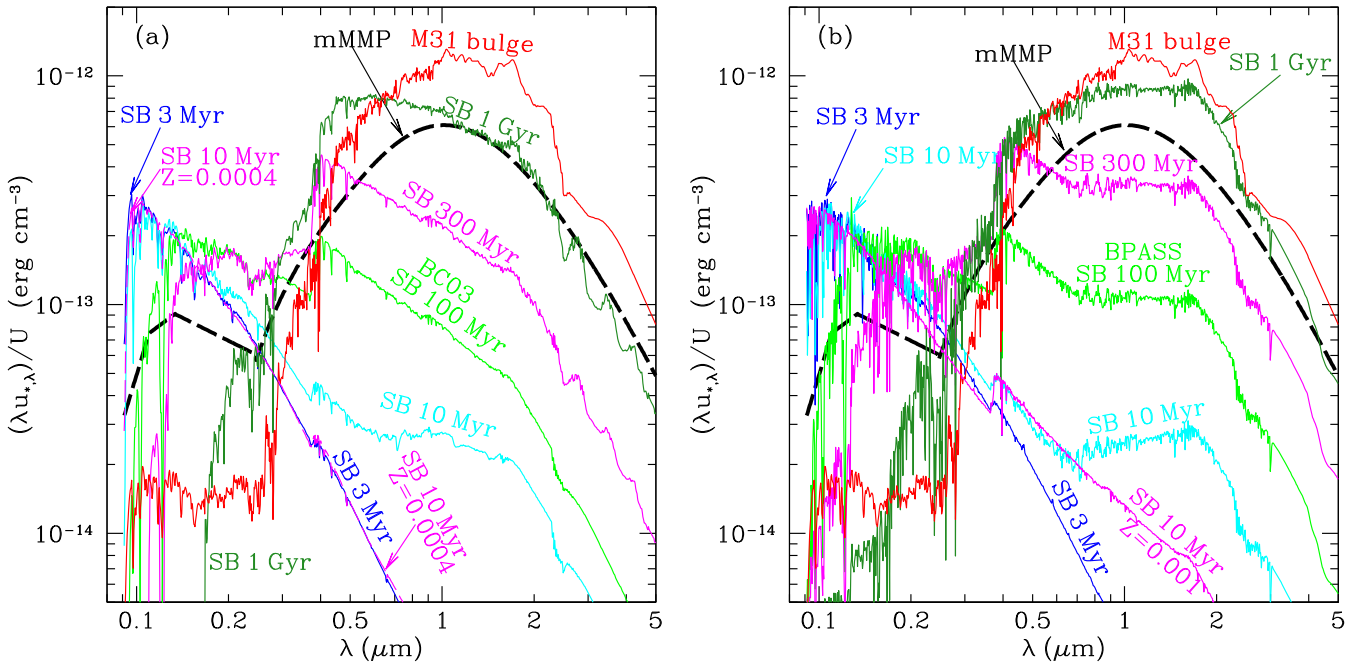

Figure 1. (a) Spectra of starlight from various stellar populations, including single-age stellar populations (Bruzual & Charlot 2003, BC03), with ages $t = 3$ Myr, 10 Myr, 100 Myr, 300 Myr, and 1 Gyr, and heavy-element mass fraction $Z = 0.02$. Also shown is the $t = 10$ Myr, $Z = 0.0004$ spectrum, very similar to the $t = 3$ Myr, $Z = 0.02$ spectrum. The black dashed curve is the mMMP spectrum of starlight in the solar neighborhood (see the text), and the red curve is the spectrum of starlight from the bulge population of M31 (Groves et al. 2012). For each spectrum, the intensity shown provides the same rate of heating $h_{\rm ref}$ for a "standard" $a = 0.1$ μm grain (see the text) as for the mMMP estimate for starlight in the solar neighborhood. (b) Same as (a), but with the BPASS single-age stellar populations (Eldridge et al. 2017; Stanway & Eldridge 2018).

Table 1
Selected Starlight Spectra

Stellar Population	Ref.	$\gamma_\star$	$u_{{\rm ref},\star}$[a] (10^{-13} erg cm^{-3})	$\langle h\nu\rangle_{\rm abs}^{\rm (Ad)}$[b] (eV)	$\langle h\nu\rangle_{\rm abs}^{\rm (PAH)}$[c] (eV)
$Z = 0.02$, $t = 3$ Myr	[d]	5.72	1.82	6.73	8.64
"	[e]	5.45	1.92	6.54	8.30
$Z = 0.0004$, $t = 10$ Myr	[d]	5.73	1.82	6.70	8.57
$Z = 0.001$, $t = 10$ Myr	[e]	5.11	2.04	6.35	8.42
$Z = 0.02$, $t = 10$ Myr	[d]	4.64	2.25	5.90	7.85
"	[e]	4.58	2.28	5.84	7.80
$Z = 0.02$, $t = 100$ Myr	[d]	2.94	3.54	4.34	5.75
"	[e]	2.55	4.09	3.94	5.69
$Z = 0.02$, $t = 300$ Myr	[d]	1.70	6.13	2.98	4.59
"	[e]	1.27	8.19	2.38	4.29
$Z = 0.02$, $t = 1$ Gyr	[d]	0.798	13.1	1.63	3.04
"	[e]	0.675	15.5	1.41	2.95
mMMP ISRF	[f]	1	10.4	1.93	4.54
M31 bulge	[g]	0.580	18.0	1.22	2.68

Notes.
[a] Energy density corresponding to $U = 1$.
[b] For $a = 0.1$ μm 1.6:1 oblate astrodust with porosity $\mathcal{P} = 0.2$ (Draine & Hensley 2021).
[c] For $N_{\rm C} = 105$ PAH$^+$.
[d] BC03 (Bruzual & Charlot 2003).
[e] BPASS (Eldridge et al. 2017; Stanway & Eldridge 2018).
[f] mMMP (Mathis et al. 1983; Draine 2011b).
[g] Groves et al. (2012).

For the starlight radiation fields of interest, such a cloud is sufficiently thick that, in the absence of scattering, the bulk of the incident starlight energy will be absorbed by dust in the cloud and reradiated in the infrared. Grains near the cloud surface will be exposed to the unreddened spectrum; grains deeper in the cloud will be heated by a weaker and redder radiation field, and thus will be cooler.

We neglect scattering, and assume unidirectional radiation incident normally on one cloud surface. We take the extinction to have the wavelength dependence A_λ/A_V adopted

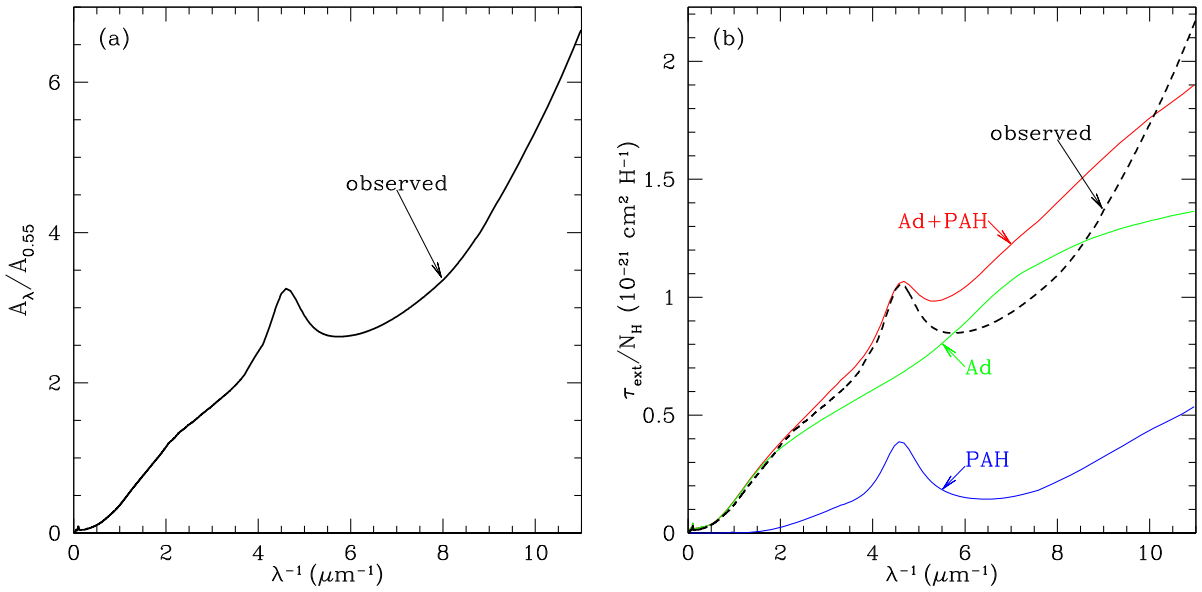

Figure 2. (a) Dust extinction in the diffuse ISM used in Equation (7) (from Hensley & Draine 2021). (b) Extinction calculated for adopted size distributions of astrodust (Ad) and PAH (Equations (14) and (15). The broken curve is observed extinction (see panel (a)).

by Hensley & Draine (2021), based largely on studies by Schlafly et al. (2016) and Fitzpatrick et al. (2019) for the diffuse interstellar medium (see Figure 2(a)). The starlight energy density per unit wavelength at a point within the cloud is taken to be

$$u_\lambda(x) = u_\lambda(0)10^{-0.4(A_\lambda/A_V)A_V x/L}, \quad (7)$$

where $0 \leqslant x \leqslant L$ is the distance from the slab surface, L is the thickness of the cloud, and A_V is the extinction at V through the cloud. Equation (7) treats scattering like absorption for estimating the attenuation of the radiation field. For normally incident radiation, this will overestimate the attenuation. On the other hand, if some or all of the incoming radiation is incident at appreciable angles relative to the normal, the attenuation law of Equation (7) will tend to underestimate the attenuation within the cloud; with these two errors tending to partially compensate, we use Equation (7) to estimate the starlight intensity within slabs with total extinction $A_V = 2$ mag.

3. PAH Physics

We idealize the PAH population as consisting of either neutral or ionized PAHs, with a size-dependent H:C ratio as assumed by Draine & Li (2007, hereafter DL07). We take the PAH nanoparticles to consist of hydrocarbon material with a carbon mass density $\rho_C = 2.0\,\mathrm{g\,cm^{-3}}$, with

$$N_C = 418\left(\frac{a}{10\ \text{Å}}\right)^3 \quad (8)$$

carbon atoms in a particle of nominal radius a.[7] We adopt the PAH cross sections $C_{abs}^{(PAH)}(a, \lambda)$ from DL07, including both optical-UV continuum and a set of resonance features, including a strong UV absorption feature at 2175 Å, and a number of infrared features corresponding to PAH vibrational modes. Because the observed 2–5 μm infrared emission from the ISM appears to include a low-level continuum underlying the PAH features (Sellgren et al. 1983; Lu et al. 2003; Helou et al. 2004; Xie et al. 2018), we follow DL07 and take the absorption cross section to be

$$C_{abs}^{PAH}(a, \lambda) = (1 - \xi_{gra})N_C\Gamma(a, \lambda) + \xi_{gra}\,C_{abs}^{(gra)}(a, \lambda)\,, \quad (9)$$

with

$$\xi_{gra} = 0.01,\ a < 50\ \text{Å} \quad (10)$$

$$= 0.01 + 0.99\left[1 - \left(\frac{50\ \text{Å}}{a}\right)^3\right],\ a > 50\ \text{Å}, \quad (11)$$

where $\Gamma(a, \lambda)$ is the "pure PAH" absorption cross section per C atom, and $C_{abs}^{(gra)}(a, \lambda)$ is the absorption cross section for graphite spheres (see Appendix A for details). Equations (9)–(11) are entirely ad hoc, to provide a small amount of "graphitic" continuum opacity so that hot PAHs can provide the continuum emission that has been observed. DL07 used the optical properties of graphite estimated by Draine (2003); here we instead use the dielectric function estimated by Draine (2016) for polycrystalline graphite using Maxwell Garnett effective medium theory.[8]

We assume that the energy $h\nu$ of an absorbed photon is fully converted to vibrational energy (i.e., "heat") in the PAH—we neglect the energy lost in the form of photoelectrons as well as possible fluorescent emission of optical photons. To calculate the temperature fluctuations, we use the heat capacity model from Draine & Li (2001), based on realistic size-dependent vibrational mode spectra for PAHs.

The interstellar PAH population likely includes a very large number of distinct PAH-like particles, in multiple charge states, including anions, neutrals, and cations. Some may be partially

[7] Our assumed PAH carbon mass density $\rho_C = 2.0\,\mathrm{g\,cm^{-3}}$ is more appropriate for real hydrocarbon solids than the crystalline graphite value $2.24\,\mathrm{g\,cm^{-3}}$ used by DL07. For example, $\rho \approx 2.0\,\mathrm{g\,cm^{-3}}$ for evaporated amorphous carbon (Fink et al. 1983).

[8] The matrix is taken to have dielectric function $\epsilon = \epsilon_\perp$, and the inclusions are taken to have $\epsilon = \epsilon_\parallel$, where $\epsilon_\perp$ and $\epsilon_\parallel$ are the eigenvalues of the dielectric tensor of crystalline graphite corresponding to $\mathbf{E}\perp c$ and $\mathbf{E}\parallel c$.

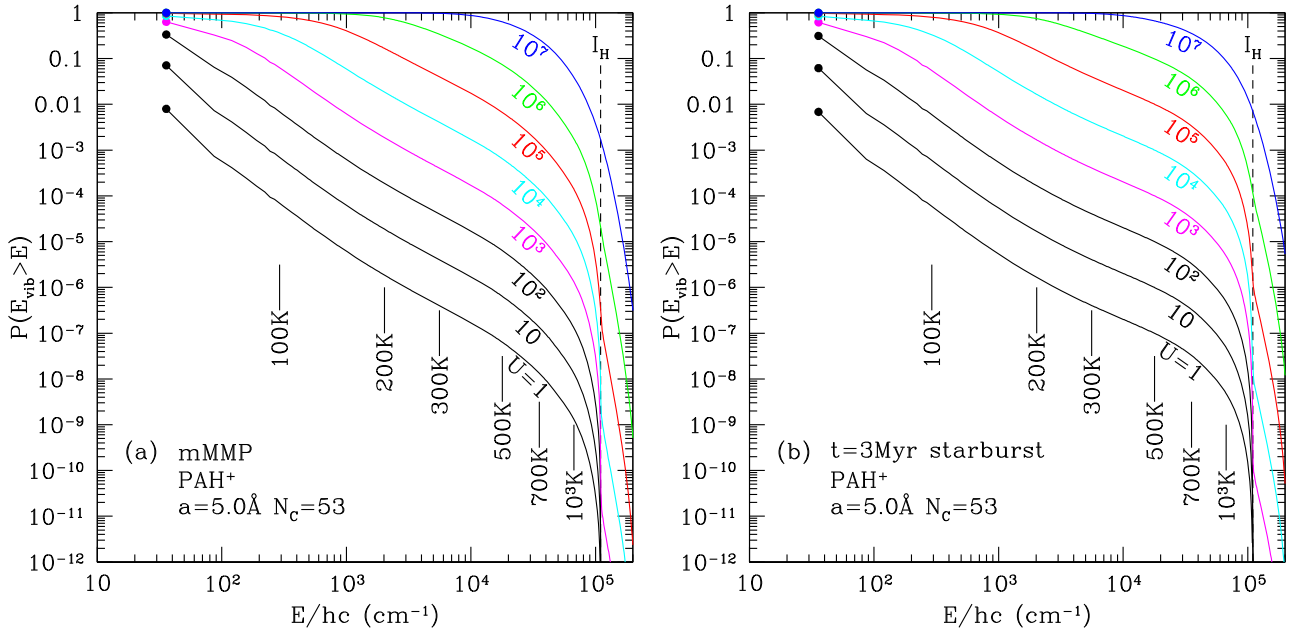

Figure 3. Probability $P(E_{\rm vib} > E)$ of having vibrational energy greater than E, for $a = 5$ Å PAH^+ in (a) mMMP interstellar radiation field (ISRF), (b) unreddened spectrum from a 3 Myr old starburst, cut off at the Lyman limit. Results are labeled by radiation strength parameter U. Vibrational energies corresponding to temperatures $T = 100$, 200, 300, 500, 700, and 10^3 K are shown. For each case, the dot indicates the location of the first energy bin above the vibrational ground state. For $U = 1$, a PAH^+ nanoparticle with $N_{\rm C} = 53$ C atoms spends ~99% of the time in the vibrational ground state, with $P(E_{\rm vib} > 0) \approx 0.01$. The vertical dashed line shows the energy $I_{\rm H} = 13.6$ eV of the highest-energy photons present in the illuminating starlight.

dehydrogenated, while others may be fully or even super-hydrogenated.

Maragkoudakis et al. (2020) have modeled the emission spectra from 308 specific PAHs, with sizes ranging from $N_{\rm C} = 22$ to $N_{\rm C} = 216$, using band strengths from density functional theory calculations in the NASA Ames PAH IR database (Bauschlicher et al. 2010; Boersma et al. 2014; Bauschlicher et al. 2018). Their approach demonstrates trends with both size and ionization, and also the considerable variation in spectra for different PAHs of similar size and ionization.

By adopting the DL07 model here, we idealize the PAHs as being characterized by a single size parameter (a or $N_{\rm C}$) and a binary charge state parameter (neutral or ionized). This is an extreme simplification, but it allows us to investigate the effects of changes in the illuminating starlight spectrum and intensity, changes in the overall PAH size distribution, and changes in the ionized fraction.

4. Temperature Distribution Functions

The compositions considered are PAH neutrals, PAH cations, and "astrodust" material. For each radiation field (spectrum and intensity), we find the steady-state energy distribution function $(dP/dE)_{j,a}$ for grains of composition j and size a. This is accomplished following the methods of Guhathakurta & Draine (1989) and Draine & Li (2001): choose an energy range $[E_{\rm min}, E_{\rm max}]$ such that the grain is very unlikely to have $E < E_{\rm min}$ or $E > E_{\rm max}$, divide this into $N = 499$ energy bins (non-uniformly spaced), calculate the transition matrix $R_{\ell k}$ giving the probability per unit time for a grain in a given bin k to make a transition to a different bin ℓ as the result of either photon absorption or photon emission, and then solve the system of equations to find the steady-state probability P_k of finding the grain in energy bin k. With each internal energy E_k, we associate a temperature $T(E_k)$, defined to be the temperature such that for a thermal distribution the expectation value of the energy would be E_k. Draine & Li (2001) showed that the instantaneous emission spectra for vibrationally excited PAHs can be adequately approximated by thermal emission.

$E_{\rm min}$ and $E_{\rm max}$ are chosen adaptively according to the grain size and radiation field; for small grains and weak radiation field, we take $E_{\rm min} = 0$ and $E_{\rm max} = 13.6$ eV, because (for $U \lesssim 10^3$) the PAH molecule spends most of its time at or close to the vibrational ground state, and single-photon heating by a starlight spectrum cutoff at 13.6 eV will not raise the grain energy by more than 13.6 eV. However, for large grains, or intense radiation fields, the vibrational energy $E_{\rm vib}$ can exceed 13.6 eV. We adjust $E_{\rm max}$ so that $P(E > E_{\rm max}) \lesssim 10^{-12}$.

Figure 3 shows cumulative energy distribution functions for PAH^+ with $N_{\rm C} = 53$ in radiation fields with intensity parameters ranging from $U = 1$ to $U = 10^7$, for the mMMP diffuse starlight spectrum (Figure 3(a)) and for the spectrum of a 3 Myr old starburst (Figure 3(b)). For $U > 10^4$, we begin to see significant populations $P > 10^{-8}$ at $E/hc > 110,000\ {\rm cm}^{-1}$ ($E > 13.6$ eV), resulting from absorption of $h\nu \approx 13$ eV photons by grains that have not yet cooled back to the ground state following a previous photon absorption.

5. Emission Spectra for Individual PAHs

5.1. Optically Thin Regions

For optically thin dust, we find the temperature distribution function $(dP/dT)_{j,a}$ and calculate the time-averaged power per unit wavelength p_λ radiated by one grain:

$$p_\lambda^{(j)}(a) = 4\pi C_{\rm abs}^{(j)}(a, \lambda) \int dT \left(\frac{dP}{dT}\right)_{j,a} B_\lambda(T), \qquad (12)$$

where $B_\lambda(T)$ is the usual blackbody function. Figure 4 shows emission per C atom from ionized and neutral PAHs of various

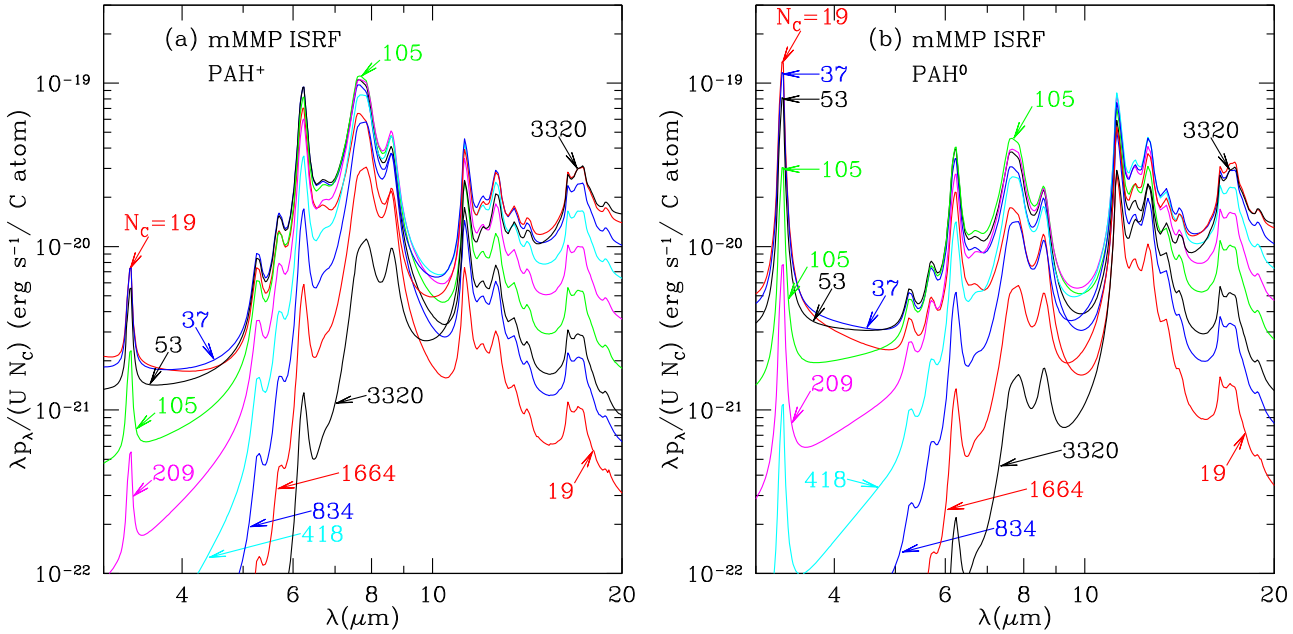

Figure 4. Emission per C atom for (a) PAH ions and (b) neutrals of various sizes, when heated by the mMMP ISRF. The spectra shown are calculated for $U = 1$, but p_λ/U is nearly independent of U for $\lambda < 20\ \mu$m and $U \lesssim 10^2$.

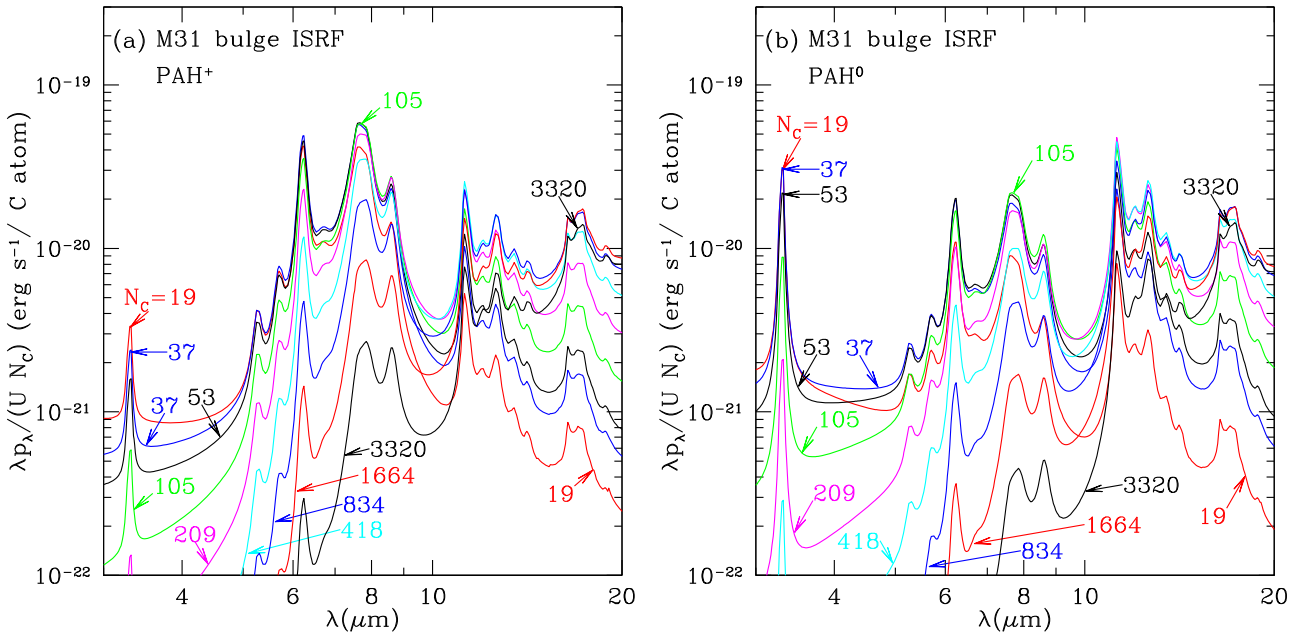

Figure 5. Same as Figure 4, but for heating by starlight from the M31 bulge population.

sizes, when illuminated by the mMMP radiation field, and Figure 5 shows the emission per grain if heated by starlight from the M31 bulge population.

Absorption of one photon can heat small PAHs to high enough temperatures that they can efficiently radiate in the shortest wavelength emission features (e.g., 3.3 μm, 5.27 μm, 5.7 μm, 6.2 μm) but larger PAHs radiate primarily in longer-wavelength features (Schutte et al. 1993). This is evident in Figures 4 and 5.

The DL07 PAH opacity model for cations includes features at 1.26 μm and 1.905 μm as recommended by Mattioda et al. (2005a). According to our models, the smaller PAH cations do emit a modest fraction of their energy in these features. These emission features appear unlikely to be observable on a galactic scale in the presence of stellar continuum at these wavelengths, but might be observable in reflection nebulae with JWST.

To better compare the relative efficiency of PAHs of different sizes for conversion of absorbed starlight energy into PAH emission features, Figure 6 shows how the strengths of various emission peaks depend on the PAH size by plotting $(\lambda p_\lambda)_{\rm peak}/p_{\rm total}$ versus $N_{\rm C}$, where $p_{\rm total} = \int d\lambda\, p_\lambda$ is the total time-averaged power radiated by the PAH. Figure 6 is similar to Figure 6 of Draine & Li (2007), differing only because of (1) differences in the treatment of the small "continuum" opacity (see Equations (9–(11)), (2) a small change in the band strengths adopted for features at 14.19 μm and the 17 μm

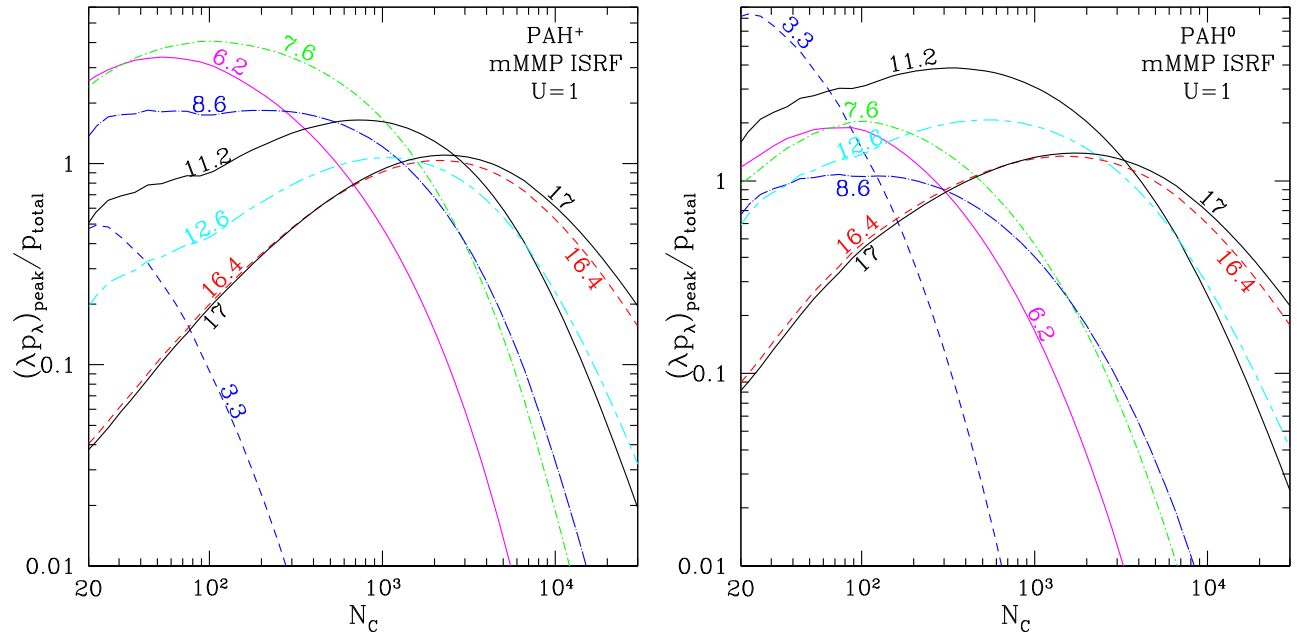

Figure 6. λp_λ evaluated at various PAH emission peaks $\lambda_{\rm peak}$, relative to the total radiated power $p_{\rm tot} = \int p_\lambda d\lambda$, as a function of the number N_C of carbon atoms in the PAH, for PAH^+ cations (left) and PAH^0 neutrals (right) heated by the mMMP starlight spectrum with $U = 1$. Curves are labeled by $\lambda_{\rm peak}$(microns).

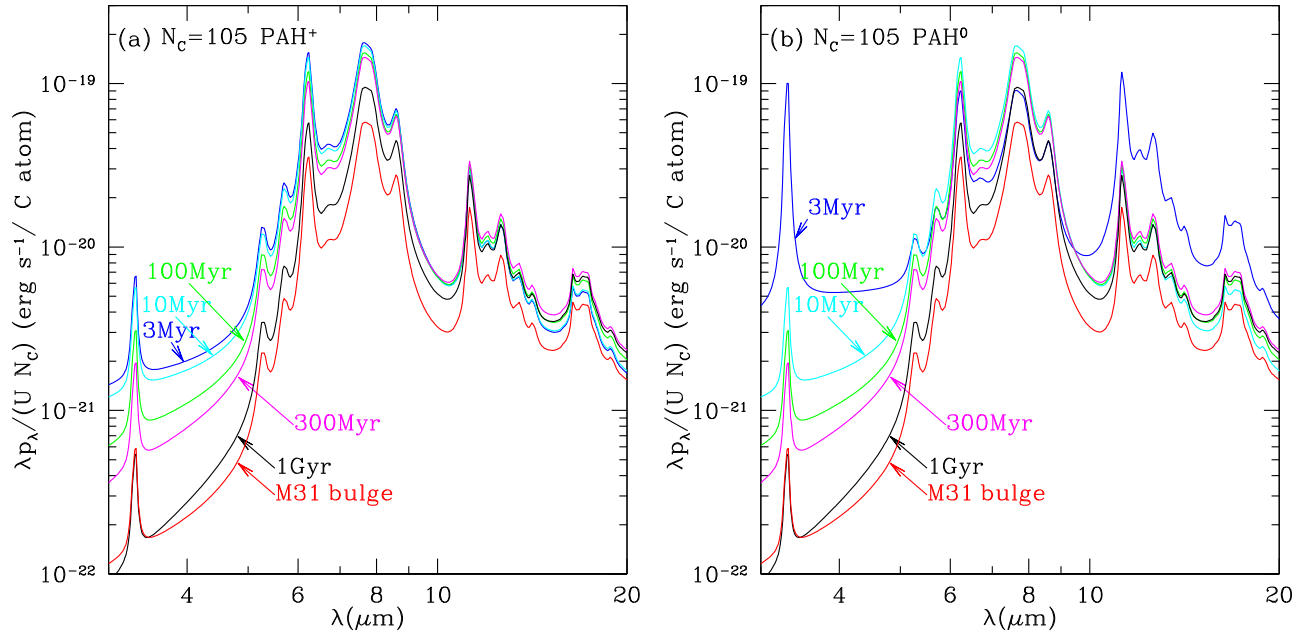

Figure 7. Emission per C atom for $N_{\rm C} = 105$ PAH^0 and PAH^+ when heated by radiation with the spectrum of the M31 bulge, and single-age $Z = 0.02$ stellar population models from BC03.

complex (see Appendix A), and (3) replacement of the Mathis et al. (1983) spectrum used by DL07 by the mMMP spectrum used here. We see that only the smallest PAH sizes ($N_{\rm C} \lesssim 100$) radiate appreciably in the 3.3 μm feature.

Schutte et al. (1993) found that PAHs with 10^2–10^5 C atoms could radiate in the IRAS 25 μm photometric band. Figure 6 shows that the 17 μm feature is efficiently radiated by large PAHs, with $N_{\rm C} \gtrsim 10^3$. The strong 7.7 μm feature is efficiently radiated by PAHs with $N_{\rm C} \approx 10^2$. This strong feature plays a large role in observational studies of PAHs; because PAHs with $N_{\rm C} > 10^3$ are relatively inefficient at radiating in this feature, DL07 defined the PAH abundance parameter $q_{\rm PAH}$ to be the ratio of the mass in PAHs with $N_{\rm C} < 10^3$ to the total mass in dust.

The time-averaged spectrum emitted by a PAH depends on the spectrum of the starlight responsible for heating the PAH. Figure 7 shows the time-averaged emission from PAH neutrals and cations with $N_{\rm C} = 105$ C atoms illuminated by different radiation fields, all with heating parameter $U = 1$. For this particular PAH size, the ratio $I(6.2\ \mu{\rm m})/I(7.7\ \mu{\rm m})$ is approximately the same for all of these radiation fields, but the ratio $I(3.3\ \mu{\rm m})/I(7.7\ \mu{\rm m})$ varies dramatically between heating by a young starburst spectrum and heating by an old stellar population (the M31 bulge spectrum). Thus interpretation of

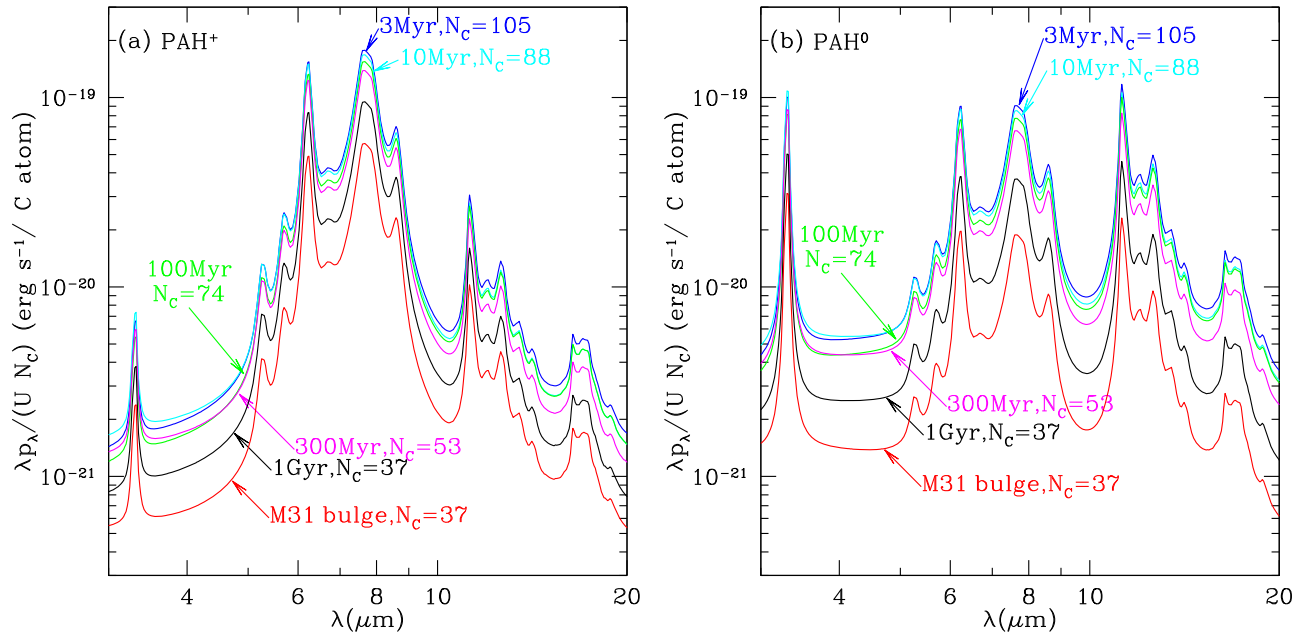

Figure 8. Emission per C atom for PAH^0 and PAH^+ when heated by various radiation fields, for sizes giving $\langle h\nu\rangle_{\rm abs}^{\rm (PAH)} = 0.08$ eV $\langle h\nu\rangle_{\rm abs}/N_{\rm C} \approx 0.08$ eV, where $\langle h\nu\rangle_{\rm abs}$ is the mean absorbed photon energy (see the text). The single-age stellar population spectra are from BC03. Except for the reddest spectra (M31 bulge and 1 Gyr old starburst), the PAH emission spectra are very similar provided $\langle h\nu\rangle_{\rm abs}^{\rm (PAH)}/N_{\rm C} \approx$ const.

PAH emission from galaxies depends on the spectrum of the starlight heating the dust.

The emission spectrum from a PAH depends on the distribution of photon energies absorbed by the PAH, but to a considerable extent it depends on a single number: the mean absorbed photon energy $\langle h\nu\rangle_{\rm abs}^{\rm (PAH)}$ per vibrational degree of freedom. A PAH containing N atoms has $3N-6$ vibrational degrees of freedom. If the illuminating spectrum is varied, so that $\langle h\nu\rangle_{\rm abs}^{\rm (PAH)}$ varies, we anticipate that the *shape* of the emission spectrum will be approximately constant if $\langle h\nu\rangle_{\rm abs}^{\rm (PAH)} \approx$ const. Ricca et al. (2012) illustrated this with $I(3.3\,\mu{\rm m})/I(11.2\,\mu{\rm m})$ versus $N_{\rm C}$ for two different initial energies.

In Figure 8 we vary $N_{\rm C}$ from 37 to 105 to keep $\langle h\nu\rangle_{\rm abs}^{\rm (PAH)}/N_{\rm C} \approx 0.08$ eV for the six different starlight spectra. Figure 8 shows the emission from neutral and ionized PAHs. The shape of the emission spectrum (e.g., $I(3.3\,\mu{\rm m})/I(11.2\,\mu{\rm m})$) is similar for all of the cases shown, as the radiation field heating the PAHs is varied from the very red M31 bulge spectrum ($\langle h\nu\rangle_{\rm abs}^{\rm (PAH)} = 2.7$ eV) to the hard UV spectrum of a 3 Myr old starburst ($\langle h\nu\rangle_{\rm abs}^{\rm (PAH)} = 8.6$ eV).

5.2. Clouds

The spectrum of the starlight heating the dust will depend on the history of star formation, but can also be affected by reddening if there is sufficient dust present so that the galaxy is not optically thin in the ultraviolet. As an example, we consider dust clouds illuminated by stars external to the cloud.

Because the starlight heating the dust is a function of depth x into the cloud (see Equation (7)), the temperature distribution function $(dP/dT)_{j,a,x}$ is a function of x in addition to depending on composition j and grain size a. To obtain the emission spectrum, we must integrate over the cloud volume. As a representative example, we consider clouds that can be approximated as slabs with total visual extinction $A_V = 2$ mag—this is large enough that most of the optical-UV energy incident on the cloud will be absorbed by dust in the cloud.

We consider a slab with $A_V = 2$ mag illuminated by radiation incident normally on one surface, with the energy density varying as in Equation (7). The emission by the dust is assumed to be optically thin. The average power per unit wavelength per grain of composition j and size a is obtained by integrating over the cloud volume:

$$\langle p_\lambda^{(j)}(a)\rangle = 4\pi C_{\rm abs}^{(j)}(a,\,\lambda)\int_0^L \frac{dx}{L}\int dT\left(\frac{dP}{dT}\right)_{j,a,x} B_\lambda(T). \quad (13)$$

6. Emission Spectra for Dust Mixtures

6.1. Size Distributions

To calculate the total dust emission, we require the size distribution and optical properties for each dust component. We assume the overall dust mass to be dominated by grains composed of a mixture of amorphous silicate, other metal oxides, and hydrocarbons—the hypothetical material termed "astrodust" by Draine & Hensley (2021) and B. S. Hensley & B. T. Draine (2021, in preparation). For astrodust we assume a porosity $\mathcal{P} = 0.20$, and the astrodust mass/H estimated by Hensley & Draine (2021) and Draine & Hensley (2021). The astrodust volume per H in the diffuse ISM in the solar neighborhood, $V_{\rm Ad} = 5.34\times10^{-27}{\rm cm}^3/{\rm H}$, is given in Table 2.

A simple power-law size distribution captures the overall balance between small and large grains, but more complex size distributions are required to reproduce the observed interstellar extinction (e.g., Kim et al. 1994; Weingartner & Draine 2001) and infrared emission (e.g., Draine & Anderson 1985; Desert et al. 1990; Li & Draine 2001; Siebenmorgen et al. 2014). Such size distributions are obtained for the "astrodust" model in a following paper (B. S. Hensley & B. T. Draine 2021, in preparation). However, to model the infrared emission from the astrodust component, here we assume a simple power-law size

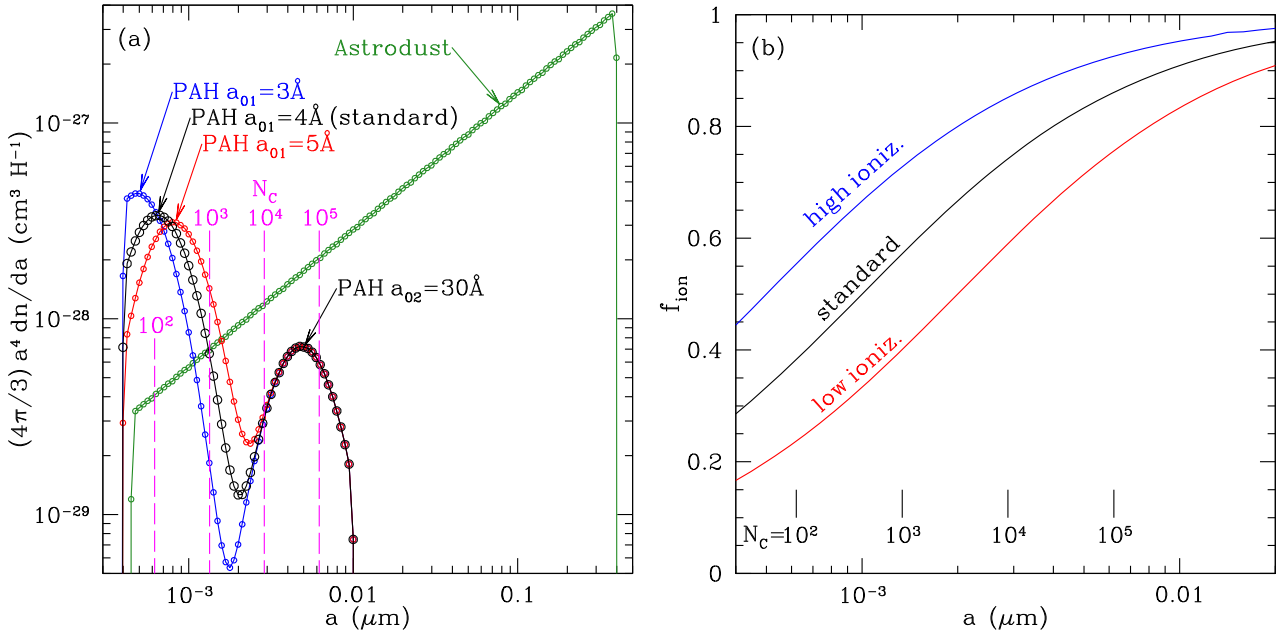

Figure 9. (a) Size distributions for astrodust and PAHs, for three different values of parameter a_{01} (see the text). Sizes corresponding to $N_C = 10^2$, 10^3, 10^4, and 10^5 are indicated. The dots show the discrete sizes used in our modeling. (b) Three examples of PAH ionization fractions (see the text).

Table 2
PAH Size Distribution Parameters[a]

Parameter	Standard Value	"Small PAHs"	"Large PAHs"
a_{01}(Å)	4.0	3.0	5.0
$B_1(10^{-7}\,\mathrm{H}^{-1})$	6.134	18.80	2.893
$q_{\rm PAH}$	0.0379	0.0391	0.0351

Note.
[a] All cases have: $a_{\rm min,\,PAH} = 4.0\times10^{-8}$ cm, $a_{\rm max,\,PAH} = 1.0\times10^{-6}$ cm, $\sigma = 0.40$, $V_{\rm PAH,1} = 3.0\times10^{-28}\,\mathrm{cm^3\,H^{-1}}$, $V_{\rm PAH,2} = 0.7\times10^{-28}\,\mathrm{cm^3\,H^{-1}}$, $a_{02} = 30$ Å, $B_2 = 3.113\times10^{-10}\,\mathrm{H^{-1}}$.

distribution

$$\frac{1}{n_{\rm H}}\frac{dn_{\rm Ad}}{da} = (4+p)\frac{(3/4\pi)V_{\rm Ad}}{a_{\rm max,Ad}^{4+p} - a_{\rm min,Ad}^{4+p}}\,a^p, \qquad a_{\rm min,Ad} < a < a_{\rm max,Ad}. \tag{14}$$

We take $p = -3.3$, $a_{\rm min,Ad} = 4.5$ Å, and $a_{\rm max,Ad} = 0.4\,\mu$m to approximately reproduce the average extinction law in the diffuse ISM. For each astrodust grain size, we calculate the probability distribution dP/dT for grain temperature. For the larger grains, dP/dT approaches a delta function.

DL07 modeled the PAH population as the sum of two log-normal size distributions:

$$\frac{1}{n_{\rm H}}\frac{dn_{\rm PAH}}{da} = \sum_{j=1}^{2}\frac{B_j}{a}\exp\left\{-\frac{[\ln(a/a_{0j})]^2}{2\sigma^2}\right\}, \qquad a_{\rm min,PAH} < a < a_{\rm max,PAH}. \tag{15}$$

About 75% of the PAH mass in the DL07 model was in a log-normal population with $a_{01} = 4.0$ Å and $\sigma = 0.40$. These are the PAH sizes that are needed to account for the observed PAH emission features. We retain this population in the present work, with a volume $V_{\rm PAH,1} = 3.0\times10^{-28}\ \mathrm{cm^3\,H^{-1}}$, containing C/H = 30 ppm.

Following DL07, we add additional carbonaceous material in a second log-normal size distribution. For this component, we take $a_{02} = 30$ Å, large enough to contribute minimal emission for $\lambda < 20\,\mu$m. We take this component to contribute a volume $V_{\rm PAH,2} = 0.7\times10^{-28}\,\mathrm{cm^3H^{-1}}$, containing C/H = 7 ppm. The two log-normal components together reproduce the observed strength of the 2175 Å feature.

Below some critical size, transient heating events will lead to "evaporation" of atoms or groups of atoms, leading to destruction of the nanoparticle. Guhathakurta & Draine (1989) estimated that graphitic clusters need to have $N_C \geqslant 23$ to survive in the ISM. We adopt a lower cutoff $a_{\rm min,PAH} = 4.0$ Å, corresponding to $N_{\rm C,min} = 27$ carbon atoms.

The size distributions are shown in Figure 9(a). The parameters in Table 2 correspond to C/H = 37 ppm in the PAH population. This differs from the value of 60 ppm adopted by DL07 because of recent findings that the extinction per H in the general diffuse ISM is smaller than previously thought.[9] For the standard parameters in Table 2, the fraction of the total dust mass contributed by PAHs containing $N_C < 10^3$ C atoms is $q_{\rm PAH} = 0.038$.

Figure 2(b) shows the extinction curve corresponding to the size distributions of Figure 9(a). The detailed wavelength dependence of extinction is not accurately reproduced, but the model extinction deviates from the observed extinction by at most ~20% (near ~1400 Å), and generally much less.

6.2. PAH Ionization

Interstellar PAHs will be present in a range of charge states, including $\mathrm{PAH^-}$ anions, neutral $\mathrm{PAH^0}$ molecules, $\mathrm{PAH^+}$ cations, and $\mathrm{PAH^{++}}$ dications. The present modeling collapses these to just PAH neutrals and PAH ions.

[9] The value of $A_V/N_{\rm H} = 3.52\times10^{-22}\ \mathrm{mag\,cm^{-2}\,H^{-1}}$ found by Lenz et al. (2017) is only 66% of the Bohlin et al. (1978) value that was long taken to be representative of the ISM in the solar neighborhood.

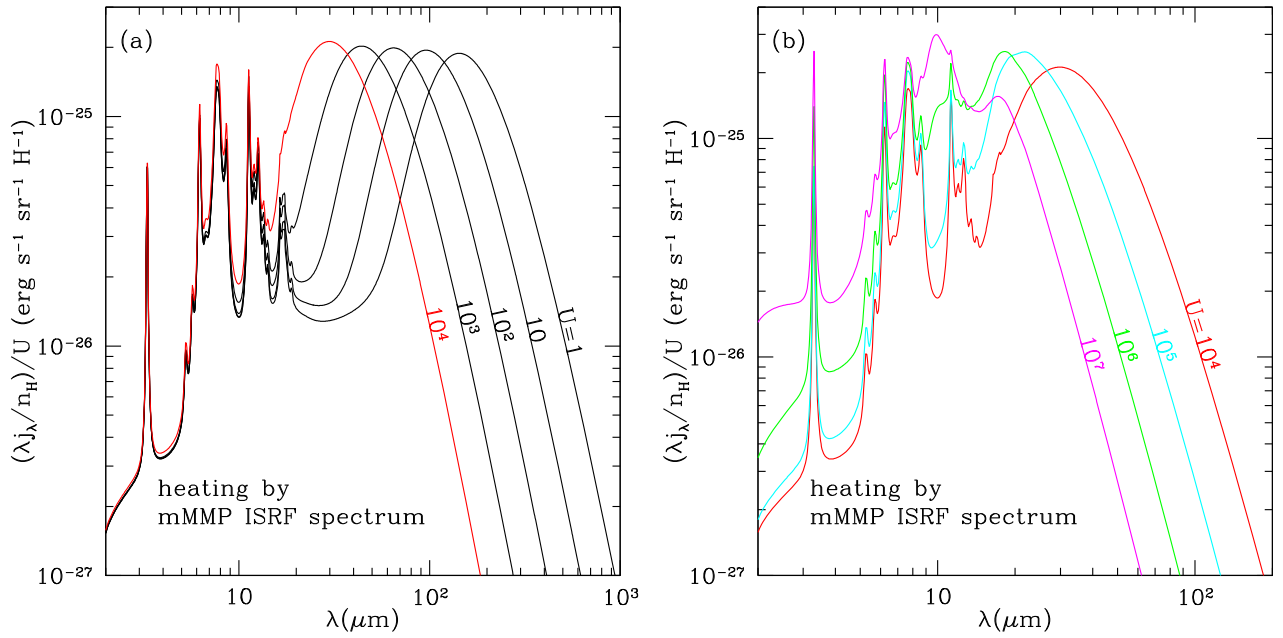

Figure 10. Emission spectra for standard dust mixture heated by radiation with mMMP ISRF spectrum and varying U, for standard PAH size distribution ($a_{01} = 4$ Å) and standard PAH$^+$ fraction $f_{\rm ion}$ (see the text). (a) $U \leqslant 10^4$; (b) $U \geqslant 10^4$.

Because PAH neutrals and ions have quite different emission spectra (compare Figures 4(a) and (b)), we must specify the PAH ionized fraction as well as the size distribution. The PAH ionization will be determined by a statistical balance between photoionizations and collisional charging by collisions with electrons and ions, and will therefore depend on electron density and electron kinetic temperature in addition to the radiation intensity. Li & Draine (2001) estimated the ionized fraction $f_{\rm ion}(a)$, as a function of PAH radius a, for three sets of physical conditions for the diffuse interstellar medium: "cold neutral medium," "warm neutral medium," and "warm ionized medium." A weighted average of these was used for the overall ISM, and this ionized fraction was adopted by DL07.

To explore the sensitivity of overall emission spectra to assumptions regarding the ionization, we will consider three examples of $f_{\rm ion}(a)$, shown in Figure 9(b). Our "standard" case is similar to $f_{\rm ion}(a)$ assumed by DL07. The high and low $f_{\rm ion}(a)$ curves in Figure 9(b) correspond to factor-of-two shifts in the PAH radius for which $f_{\rm ion} = 0.5$. Because the photoionization rate for a neutral PAH scales approximately as Ua^3, and the electron capture rate for a PAH cation scales approximately as $a^2 n_e/\sqrt{T_e}$, a shift of a factor of two in the size where $f_{\rm ion} = 0.5$ corresponds approximately to a factor-of-two shift in the ratio $Ua\sqrt{T_e}/n_e$. It would not be surprising if even larger variations in PAH ionization occurred. The relative constancy of PAH spectra may therefore be an indication of self-regulation in the ISM that limits variations in $U\sqrt{T_e}/n_e$.

6.3. Diffuse ISM

Let $4\pi j_\lambda$ be the power radiated per unit volume, per unit wavelength. The emissivity per H nucleus is obtained by summing the radiated power per grain over the grain size distribution:

$$\frac{4\pi j_\lambda}{n_{\rm H}} = \sum_j \int da \left[\frac{1}{n_{\rm H}}\frac{dn_j}{da}\right] p_\lambda^{(j)}(a). \qquad (16)$$

Figure 10 shows emission spectra calculated for the standard dust mixture heated by starlight with the mMMP spectrum, but varying U. At FIR wavelengths, the opacity of astrodust varies approximately as $\lambda^{-1.8}$ (Hensley & Draine 2021). Therefore, as U is increased, the temperature of the large grains increases as $T \propto U^{1/5.8}$, with the wavelength where λp_λ peaks in the FIR varying as

$$\lambda_{\rm FIR\ peak} \approx 140\ \mu{\rm m} \times U^{-1/5.8} \ \text{for}\ U \lesssim 10^4. \qquad (17)$$

At the same time, for $U \lesssim 10^3$, the *shape* of the emission spectrum at $\lambda \lesssim 15\ \mu$m remains nearly invariant, with the emission remaining dominated by cooling following single-photon heating. Only as U exceeds $\sim 10^3$ does the heating become sufficient to modify the shape of the $\lambda < 15\ \mu$m emission, but the spectrum for $\lambda < 10\ \mu$m remains unaffected even for $U = 10^4$.

For $U \gtrsim 10^5$, the silicate features begin to appear in the emission spectrum (see Figure 10(b)), as the astrodust grains become warm enough ($T \gtrsim 130$ K) to radiate strongly in the 18 μm feature and, for $U \gtrsim 10^6$, in the 9.7 μm feature as well. For $U \gtrsim 10^6$, the silicate 10 μm emission feature is comparable to or stronger than the strongest PAH emission features.

The normalized emission $\lambda j_\lambda \Big/ \left[\int j_\lambda\, d\lambda\right]_{\rm TIR} = \lambda L_\lambda / L_{\rm TIR}$, where $L_{\rm TIR}$ is the total infrared power, is shown for the standard dust mixture in Figure 11 for three different starlight spectra. Results for $U = 1$ are shown in Figure 11(a), and for $U = 10^3$ in Figure 11(b).

The mMMP and M31 bulge spectra both have $\lambda_{\rm FIR\ peak} \approx 140\ \mu$m for $U = 1$, but the 3 Myr old starburst spectrum has $\lambda_{\rm FIR\ peak} \approx 130\ \mu$m, showing that the single parameter U does not completely capture the heating effects of the radiation field on a dust mixture—the shape of the spectrum also matters. Recall that U was defined in terms of the rate of heating of $a_{\rm eff} = 0.1\ \mu$m astrodust grains. For the standard dust mixture, the FIR emission from $a_{\rm eff} \approx 0.1\ \mu$m

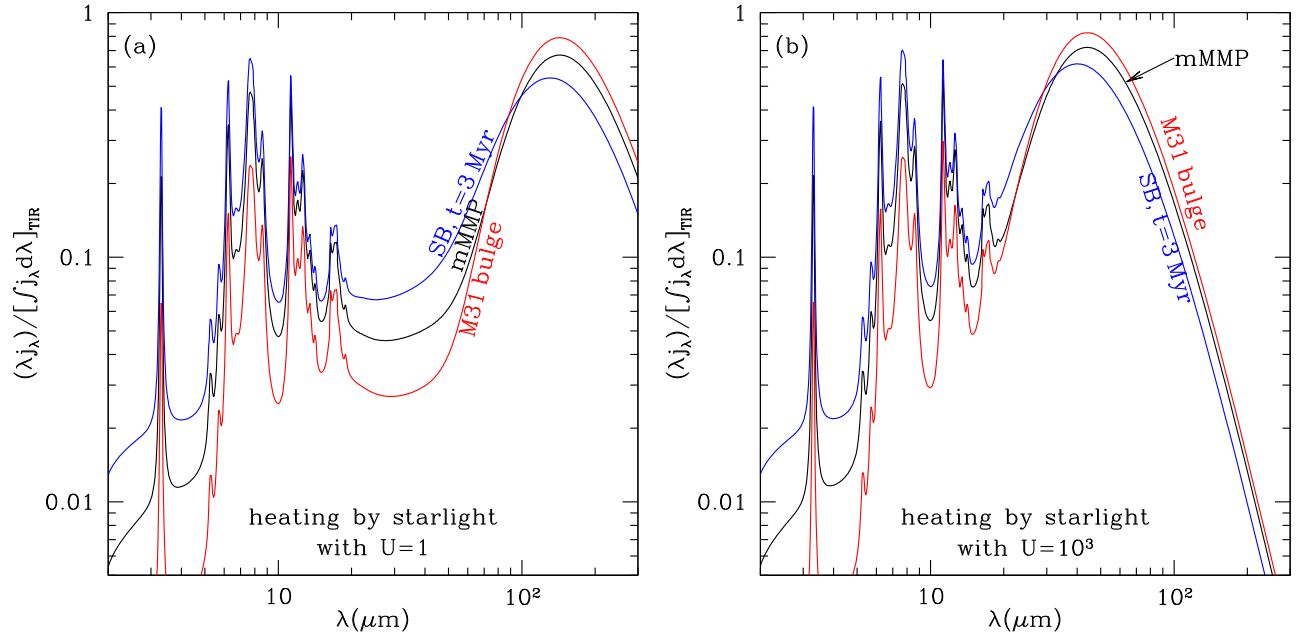

Figure 11. Normalized emission spectra for standard dust mixture heated by different starlight spectra with $U = 1$ (left) and $U = 10^3$ (right).

dust appears to be representative of the broad FIR peak when the dust is heated by starlight spectra that are broadly similar to the mMMP spectrum. However, a very young starburst has a starlight spectrum with far more energy in the far-UV (see Figure 1), which has the effect of increasing the fraction of the starlight absorption contributed by the smaller grains. The smaller grains are somewhat warmer, hence the peak of the SED is at $\sim$130 μm for $U = 1$ rather than $\sim$140 μm as for the mMMP and M31 bulge spectra. Increasing U to $U = 10^3$ shifts $\lambda_{\rm FIR\ peak}$ to $\sim$42 μm for the mMMP spectrum.

The PAH emission features are sensitive to the starlight spectrum. For our standard dust mixture, Figure 11 shows that the 3 Myr old starburst spectrum produces normalized PAH features that are $\sim$20% stronger than for heating by the mMMP spectrum, while heating by the M31 bulge spectrum produces normalized PAH features that are a factor of $\sim$2 weaker than for the mMMP spectrum, as previously found by Draine et al. (2014). The PAH band ratios (e.g., $F(3.3\ \mu{\rm m})/F(11.2\ \mu{\rm m})$) are sensitive to the spectrum of the illuminating starlight, and vary significantly as the radiation field is varied from a 3 Myr old starburst spectrum to the very red M31 bulge spectrum. The dependence of band ratios on the starlight spectrum is discussed below in Section 9.7.

6.4. Clouds

Because the starlight heating the dust is a function of depth x into the cloud (see Equation (7)), the temperature distribution function $(dP/dT)_{j,a}$ is a function of x, and we must therefore average over the cloud volume. The infrared emission is assumed to be optically thin. The cloud-averaged emissivity per H is

$$\left\langle \frac{4\pi j_\lambda}{n_{\rm H}} \right\rangle = \sum_j \int da \frac{1}{n_{\rm H}} \frac{dn_j}{da} \langle p_\lambda^{(j)}(a) \rangle. \tag{18}$$

with the cloud-averaged $\langle p_\lambda^{(j)}(a) \rangle$ given by Equation (13). Figure 12 shows normalized emission spectra for diffuse dust heated by starlight with $U = 10^3$, and for a dust cloud with $A_V = 2$ exposed to the same radiation field at the cloud surface. Figure 12(a) is for starlight with the mMMP spectrum, appropriate for a mature star-forming galaxy. As expected, the FIR peak shifts from $\lambda_{\rm FIR\ peak} \approx 40\ \mu$m for the diffuse ISM starlight to $\sim$50 μm for the cloud, because most of the starlight power absorbed in the clouds takes place in an attenuated (and reddened) radiation field, with dust temperatures somewhat lower than at the cloud surface. The 3.3 μm PAH feature drops by about a factor of two, because excitation of the 3.3 μm feature is dependent on the more energetic stellar photons, and these are attenuated relatively rapidly as one moves into the dust slab.

Figure 12(b) shows the same calculation, but now for a radiation spectrum characteristic of a 3 Myr old starburst and $U = 10^3$. Once again, attenuation within the cloud shifts the peak of the FIR emission longward by about a factor 1.2, but for this case the normalized PAH features are nearly unchanged. This is because *most* of the starlight energy is in the UV, and capable of exciting the PAH features via single-photon heating. Because the incident radiation field is dominated by FUV photons, the PAH excitation falls off like the overall dust heating rate, leaving the *ratio* of PAH emission to total emission almost unaffected. We will see below (in Section 9.2) that the PAH band ratios remain nearly unchanged by reddening when the unreddened starlight is dominated by UV.

Figure 13(a) shows how $\lambda_{\rm FIR\ peak}$ depends on the heating parameter U, and on the spectrum of the starlight. The wavelength $\lambda_{\rm FIR\ peak}$ depends primarily on U (see Equation (17)), but $\lambda_{\rm FIR\ peak}$ does depend slightly on the spectrum of the radiation heating the dust. Figure 13(b) shows $\lambda_{\rm FIR\ peak}$ for emission from an $A_V = 2$ mag cloud, as a function of the parameter U for the radiation at the cloud surface. The emission from the cloud includes radiation from dust grains heated by the attenuated radiation field within the cloud, which shifts $\lambda_{\rm FIR\ peak}$ longward of where it would be for only the emission from the grains at the cloud surface. Figure 13

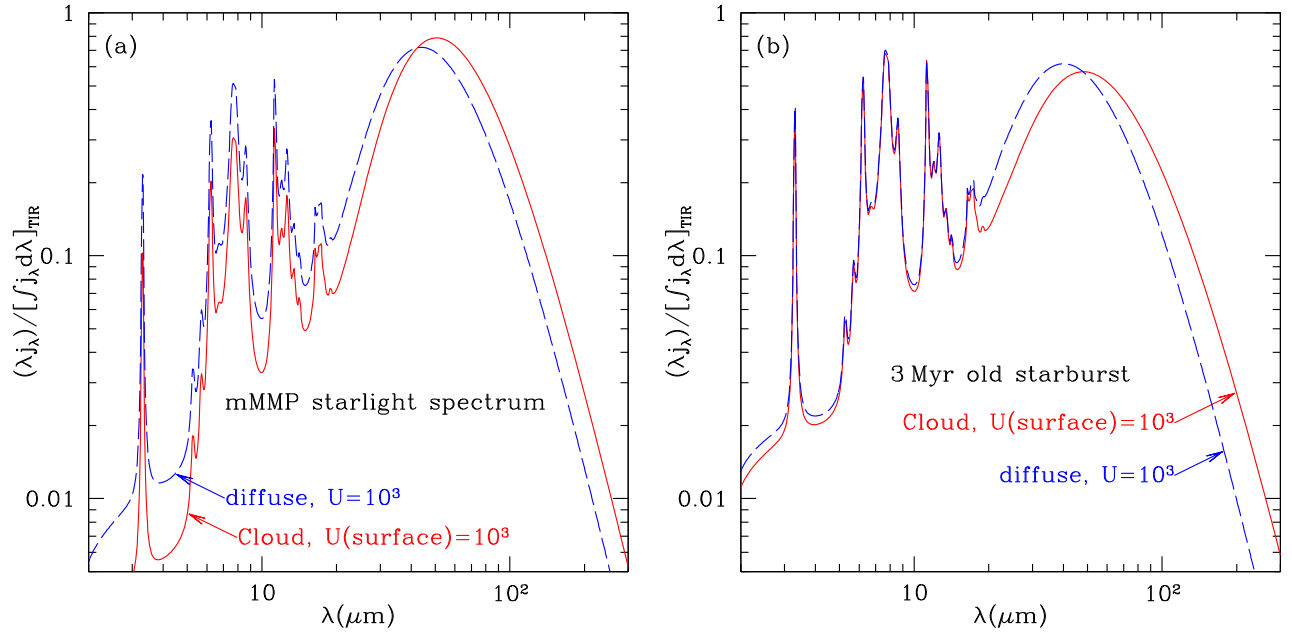

Figure 12. Emission (normalized to total infrared, TIR) from diffuse dust exposed to starlight with $U = 10^3$, and from a dust slab with $A_V = 2$ mag. (a) Incident starlight with mMMP ISRF spectrum. The PAH features for the slab are weakened by a factor ~1.5. (b) Incident starlight from 3 Myr old starburst. The normalized PAH features are almost unaffected by reddening, because most of the stellar power is in the far-UV.

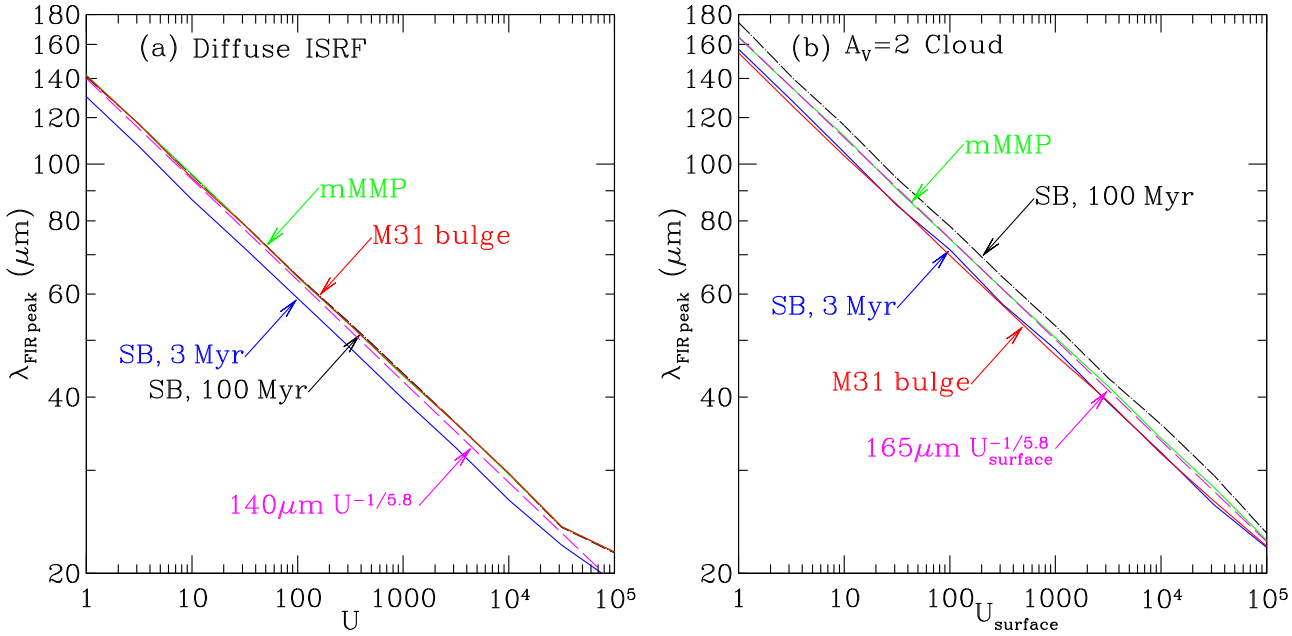

Figure 13. Wavelength $\lambda_{\rm FIR\ peak}$ where λj_λ peaks in the far-infrared, as a function of starlight heating parameter U, for our standard model and various radiation fields. (a) Unattenuated radiation fields. (b) Emission summed over a cloud with $A_V = 2$. In each panel, the magenta dashed line is a power-law fit.

shows that this shifts $\lambda_{\rm FIR\ peak}$ longward by about a factor 1.2 for the mMMP spectrum.

7. Sensitivity to Ionized Fraction

The emission spectrum of a vibrationally excited PAH depends on whether the PAH is neutral or ionized. Laboratory measurements and theoretical calculations for small PAHs find that the band strengths for some of the important spectral features depend strongly on the ionization state (DeFrees et al. 1993; Allamandola et al. 1999). PAH^+ cations have smaller band strengths for the C–H stretch at 3.3 μm than the corresponding neutral PAH. Conversely, the C–C stretching modes at 6.2 and 7.7 μm have larger band strengths for PAH^+ cations than for the corresponding neutral PAHs.

Our present calculations are based on the PAH band strengths adopted by DL07; for the 3.3 μm C–H stretching feature, for example, neutral PAHs are assumed to have a band strength 4.4 times larger than for the corresponding PAH^+ cation, while the band strength for the 7.7 μm feature is taken to be nine times larger for cations than for neutrals. The values adopted by DL07 are consistent with the range in results found in theoretical calculations (e.g., Malloci et al. 2007;

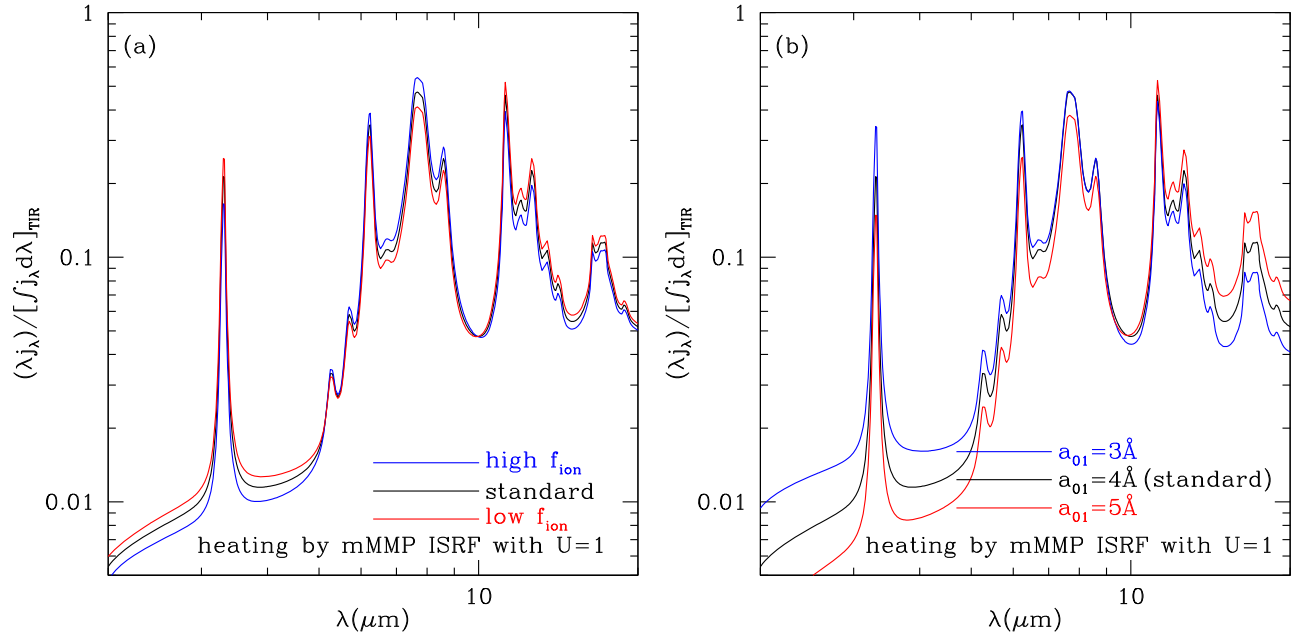

Figure 14. Emission spectra (normalized to total infrared emission) (a) for standard dust mixture heated by mMMP starlight spectrum, for three different PAH ionized fractions $f_{ion}(a)$ (see the text). (b) Three different PAH size distributions, parameterized by a_{01} (see the text).

Bauschlicher et al. 2010, 2018), and are intended to represent general trends for the actual PAH-like nanoparticles in the ISM.

As a result, the model emission spectrum depends on the assumed fractional ionization of the PAHs, which will be dependent on local conditions: the intensity of UV photons capable of photoionizing the PAHs, and the density and temperature of the free electrons that can be captured by the PAHs. Because the PAH ionization must depend on local conditions, one may expect regional variations in PAH emission spectra arising from variations in the degree of ionization of the PAHs.

Our standard dust model above included an assumption of how the PAH ionization fraction depends on the PAH size (see Figure 9(b)). Here we examine how varying $f_{ion}(a)$ affects the relative strengths of PAH features after integrating over the size distribution. Figure 14(a) shows model emission spectra for dust heated by the mMMP radiation field, for the three different levels of PAH ionization shown in Figure 9(b). As expected, increasing (decreasing) the ionization increases (decreases) the 7.7 μm/3.3 μm and 7.7 μm/11.2 μm band ratios. This will be further explored in Section 9.5 below.

8. Sensitivity to PAH Size Distribution

Single-photon heating raises smaller PAHs to higher peak temperatures than larger PAHs. Because emission in the shorter wavelength PAH bands can only be excited when the nanoparticle is quite hot, the infrared emission spectrum is sensitive to the PAH size distribution.

The PAH size distribution is the result of competing processes including fragmentation of large grains, chemisputtering by reaction with radicals, physical sputtering in hot gas, photodesorption of atoms or complexes, growth by accretion of individual atoms, agglomeration with either other nanoparticles or larger grains, and perhaps other processes. Unfortunately, at this time our limited theoretical understanding of these processes cannot provide a credible a priori expectation for the shape of the size distribution, other than that we expect a fairly sharp cutoff at the smallest sizes because below some critical size, particles cannot survive in the UV radiation field.

Changes in the PAH size distribution could be accompanied by changes in the character of the PAHs. PAH emission spectra have been classified by Peeters et al. (2002) based on the 6–9 μm spectrum. Integrated spectra of galaxies generally fall into class A, but individual regions (e.g., planetary nebulae, Herbig Ae-Be stars, post-AGB stars) are often in classes B or C. An additional class D was introduced by Matsuura et al. (2014) to accommodate the spectra of certain post-AGB stars in the LMC.

Shannon & Boersma (2019) proposed that classes A and B may differ in part because of the sizes of the PAHs emitting in the 6–9 μm region, with class B PAHs being larger. Shannon & Boersma (2019) calculated the emission from PAHs excited by monochromatic 5 eV photons. Here we use a full spectrum of exciting radiation; we also examine the complete 3–20 μm spectra.

Our adopted "standard" size distribution (see Figure 9(a) and Equation (15)) is an empirical distribution, adopted by DL07 because it seemed to do a good job of reproducing observed 5–20 μm PAH spectra of galaxies (e.g., Smith et al. 2007), if the PAHs are assumed to be heated by radiation with the spectrum of the mMMP interstellar radiation field (ISRF).

To investigate the sensitivity of the model spectra to the size distribution, we arbitrarily change the parameter a_{01} by $\pm 25\%$, corresponding to increasing the characteristic mass $\propto a_{01}^3$ by $1.25^3 = 1.95$, or reducing it by a factor $0.75^3 = 0.42$. In Figure 14(b) we see that even such small variations in PAH size result in appreciable changes in PAH band ratios: as expected, reducing a_{01} results in an increase in the 3.3 μm/7.7 μm band ratio, because the smallest PAHs are more readily excited to the high temperatures required for appreciable emission at 3.3 μm. The effects on band ratios are discussed further in Section 9.7.

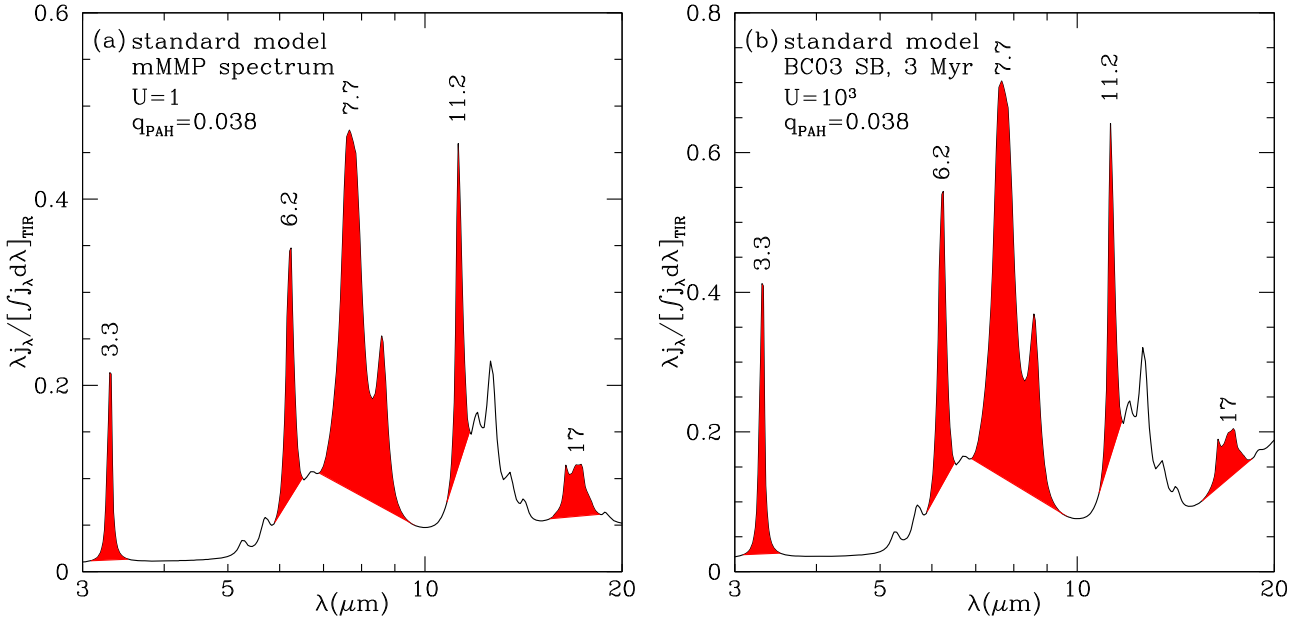

Figure 15. Normalized emission spectra for our standard model. (a) For the mMMP starlight spectrum with $U = 1$. The red line indicates the baselines used for extraction of the power in various emission features. (b) For heating by the $h\nu < 13.6$ eV radiation from a 3 Myr old starburst, with $U = 10^3$.

9. Discussion

The emission spectra p_λ calculated here are available online.[10] for a grid of grain sizes and starlight intensities, and for selected spectral shapes for the starlight heating the dust. We also make available emission spectra for complete dust models for three possible PAH size distributions (see Figure 9(a)), and for three possible PAH ionization fractions $f_{\rm ion}(a)$ (see Figure 9(b)). These emissivities can be used for modeling the emission from galaxies containing distributions of starlight intensities.

9.1. Feature Strengths

Interpretation of the emission features in observed infrared spectra requires quantitative determination of the feature strengths. Feature "extraction" is complicated by the presence of a "continuum," and because the features may be overlapping in wavelength. In addition, the observed emission may be affected by extinction, particularly in the 9.7 μm silicate feature, which should be corrected for (Smith et al. 2007).

Various approaches have been taken. Some studies employ spline fits to the presumed continuum so that it can be subtracted to reveal the emission features (e.g., Peeters et al. 2002; Brandl et al. 2006). Another approach is to fit the observed spectra, including the continuum, using a physically motivated set of fitting functions with a tractable number of free parameters; PAHFIT (Smith et al. 2007) is one such spectral-fitting code. Different feature extraction techniques may differ appreciably in estimation of the power in the different PAH bands. Paper II (J.-D. T. Smith et al. 2021, in preparation) applies an expanded PAHFIT decomposition to our model spectra.

Component-fitting procedures such as PAHFIT provide the best measure of the power F radiated in a spectral feature, but require sophisticated fitting of a multicomponent model to the measured spectra. Since our modeled emission spectra do not include contributions from direct starlight, line emission, differential attenuation of the emission by dust (with the 10 μm silicate feature), and emission from other hot dust (e.g., from active galactic nuclei), a simpler approach can illustrate the main trends. Here we adopt a very simple method, to obtain the "clipped" flux $F_{\rm clip}$ in a feature: we specify points λ_1 and λ_2 on either side of the feature where the feature strength will be taken to be zero, define a "clip-line" $\lambda F_\lambda^{\rm (c.l.)}$ between these two wavelengths to be a linear function of $\log\lambda$ connecting λF_λ at the clip points (see Figure 15), and define

$$F_{\rm clip}({\rm band}) \equiv \int_{\lambda_1}^{\lambda_2} (F_\lambda - F_\lambda^{\rm (c.l.)}) d\lambda. \quad (19)$$

Our adopted "clip points" λ_1, λ_2 for each feature or "band" are given in Table 3. We treat the broad 7.7 μm complex (with overlapping sub-features at 7.417, 7.598, and 7.85 μm) *and* the 8.6 μm feature as a single "7.7 μm" feature extending from 6.9 to 9.7 μm. Similarly, we aggregate emission features at 15.9, 16.4, 17.04, and 17.375 μm into a single "17 μm" feature extending from 15.5 to 18.5 μm. Values of $F_{\rm clip}({\rm band})/F_{\rm TIR}$ for our standard model heated by the mMMP ISRF with $U = 1$ are given for five features in Table 3.

Table 3
Selected PAH Emission Components

Feature	Clip Points λ_1 (μm)	Clip Points λ_2 (μm)	$F_{\rm clip}/F_{\rm TIR}$[a]
3.3 μm	3.09	3.52	0.0044
6.2 μm	5.90	6.50	0.0130
7.7 μm	6.90	9.70	0.0394
11.2 μm	10.80	11.70	0.0103
17 μm	15.50	18.50	0.0061

Note.
[a] Standard model ($q_{\rm PAH} = 0.0379$), mMMP starlight, $U = 1$.

[10] Data are available for download from https://doi.org/10.7910/DVN/LPUHIQ.

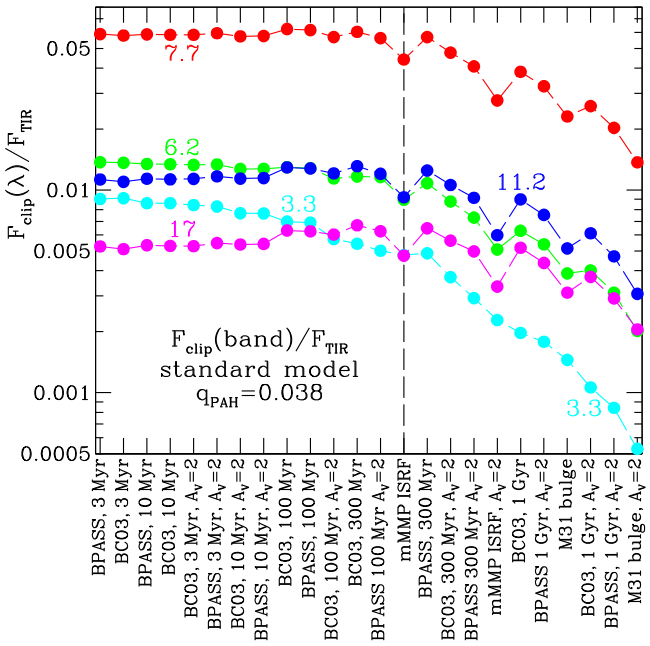

Figure 16. Normalized "clipped" band strengths for the 3.3, 6.2, and 11.2 μm features, and for the 7.7 and 17 μm complexes (see Figure 15). Models are calculated for unattenuated starlight spectra with $U = 1$, and for $A_V = 2$ clouds with $U_{surface} = 1$. Cases are shown in order of decreasing $F_{clip}(3.3)/F_{TIR}$.

Figure 15(a) shows our model spectrum for dust heated by the mMMP starlight spectrum, with our standard PAH size distribution, and our standard PAH ionization fraction f_{ion}; Figure 15(b) shows the same dust model but heated by starlight with the spectrum of a 3 Myr old starburst and heating parameter $U = 10^3$. We examine the strengths of the five features listed in Table 3. Figure 15 shows these five features with the adopted baselines. Because the real feature profiles may have broad wings (note the substantial power below the red "features" in Figure 15), the present approach will significantly underestimate the actual power in the features. The present approach does, however, provide a simple systematic way to quantify feature strengths, thereby allowing us to discuss variations of those feature strengths, and to compare to observed spectra.

9.2. Sensitivity to Starlight Spectrum and Reddening

The sensitivity of the different emission bands to the spectrum of the starlight heating the dust and PAHs is explored in Figure 16, which shows feature strengths (normalized by the total IR power) $F_{clip}(band)/F_{TIR}$ for 24 different examples of starlight heating. All cases are for $U = 1$, but 12 different starlight spectra are considered. For each starlight spectrum, we compute the IR emission for diffuse dust, and also for dust in $A_V = 2$ mag clouds with the starlight incident on the cloud surface. For each of the single-age stellar populations (3, 10, 100, 300 Myr, and 1 Gyr), we consider both BC03 (Bruzual & Charlot 2003) and BPASS (Eldridge et al. 2017; Stanway & Eldridge 2018) stellar models. In Figure 16 the cases are ordered by decreasing fractional power in the 3.3 μm feature.

As the (unreddened) radiation spectrum varies from a 3 Myr old starburst to the M31 bulge, $F_{clip}(3.3)/F_{TIR}$ drops by a factor $\sim$6, from 0.91% to 0.15%. Other bands are less sensitive—$F_{clip}(7.7)/F_{TIR}$ declines by only a factor $\sim$2.5, from 5.8% to 2.3%. Thus band ratios such as $F_{clip}(3.3)/F_{clip}(7.7)$ are sensitive to the illuminating spectrum, as will be further examined below.

For the "cloud" cases, reddening of the starlight within the cloud results in the total emission from the cloud having fractional band powers F_{clip}/F_{TIR} that are lower than the values for the unreddened incident spectrum. For example, compare the mMMP ISRF and mMMP ISRF, $A_V = 2$ cases in Figure 16: $F_{clip}(3.3\ \mu m)/F_{TIR}$ is lower by a factor of $\sim$2 for the $A_V = 2$ cloud. However, if the incident starlight spectrum is dominated by UV, as for starbursts with ages $\lesssim$10 Myr, reddening leads to only a small decrease in $F_{clip}(band)/F_{TIR}$, because the starlight power is dominated by far-UV radiation—the PAHs and the dust are heated by the same photons. Even the UV-sensitive 3.3 μm band is minimally affected: $F_{clip}(3.3\ \mu m)/F_{TIR}$ is reduced by only 10% in going from unreddened BC03 3 Myr radiation to the case of an $A_V = 2$ cloud (see Figure 16).

9.3. q_{PAH} Estimation

The PAH abundance q_{PAH} can be estimated from the strength of the observed PAH emission features. q_{PAH} estimation is usually done using the 7.7 μm feature, because it is the strongest, and also because it was well-matched to band 4 of the Infrared Array Camera (Fazio et al. 2004), allowing the 7.7 μm feature to be measured efficiently by the Spitzer Space Telescope. q_{PAH} is taken to be proportional to the fraction of the total IR power appearing in the 7.7 μm feature:

$$q_{PAH} = R^{clip}_{q_{PAH}} \times \frac{F_{clip}(7.7)}{F_{TIR}}, \tag{20}$$

where the factor $R^{clip}_{q_{PAH}}$ is obtained by modeling the PAH emission spectrum from a model with known q_{PAH} (e.g., Table 3). In this paper we extract feature fluxes F_{clip} using the simple method described in Section 9.1. The factor $R^{clip}_{q_{PAH}}$ will in general depend on the spectrum of the starlight responsible for heating the PAHs and dust, and also on both the state of ionization and the size distribution of the PAHs.

Figure 17(a) shows $R^{clip}_{q_{PAH}}$ for a number of different starlight spectra, and for three different assumed PAH ionization functions f_{ion}. While $R^{clip}_{q_{PAH}}$ varies among the different starlight spectra, it is gratifying to see that the variations in $R^{clip}_{q_{PAH}}$ are modest over a wide range of starlight spectra that might be appropriate in star-forming galaxies, ranging from a very young 3 Myr old starburst to a 300 Myr old starburst, with the mMMP radiation field falling in between: we can generally take $R^{clip}_{q_{PAH}} \approx 0.8^{+0.3}_{-0.25}$ provided that the stellar population is not extremely evolved. For the very extreme case of the starlight from the M31 bulge population, we have $R^{clip}_{q_{PAH}} \approx 1.6$; if this starlight is reprocessed by dust clouds with $A_V \approx 2$, $R^{clip}_{q_{PAH}}$ rises to $R^{clip}_{q_{PAH}} \approx 2.8$.

Figure 17(a) shows that variations in the PAH ionization also affect $R^{clip}_{q_{PAH}}$, because PAH neutrals do not radiate as strongly as PAH cations in the 7.7 μm C–C band. Thus the low f_{ion} models have higher $R^{clip}_{q_{PAH}}$ values than the standard model. However, $R^{clip}_{q_{PAH}}$ is more sensitive to changes in the starlight spectrum than to variations in f_{ion}.

The sensitivity of $R^{clip}_{q_{PAH}}$ to the assumed size distribution is examined in Figure 17(b). $R^{clip}_{q_{PAH}}$ varies by only $\sim\pm5\%$ for $a_{01} = 4 \pm 1$ Å. From Figure 17 we see that if we have a good way to estimate the spectrum of the starlight exciting the PAH

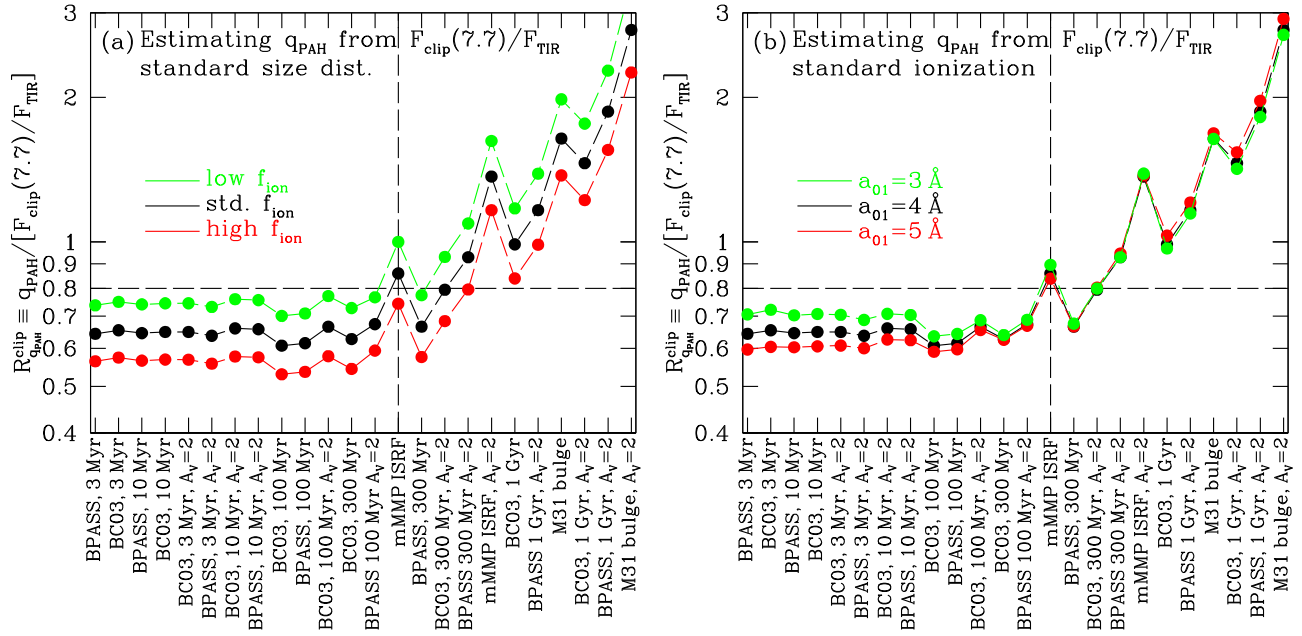

Figure 17. $R^{clip}_{q_{PAH}} \equiv q_{PAH}/[F_{clip}(7.7)/F_{TIR}]$, where $F_{clip}(7.7)$ is extracted as shown in Figure 15. (a) Standard size distribution, for a range of radiation fields (see the text), and three different assumptions about the PAH ionization f_{ion} (see Figure 9(b)). For radiation fields appropriate to star-forming galaxies, $R^{clip}_{q_{PAH}} \approx 0.8^{+0.3}_{-0.25}$, allowing q_{PAH} to be estimated reliably from the measured $F_{clip}(7.7)/F_{TIR}$. However, for very red starlight spectra (e.q., M31 bulge), $R^{clip}_{q_{PAH}}$ increases, because $F_{clip}(7.7)/F_{TIR}$ is suppressed. (b) Standard ionization, for a range of radiation fields, and three different values of a_0 (see Figure 9(a)).

emission, we can estimate q_{PAH} to within $\sim\pm10\%$ accuracy from $F_{clip}(7.7)/F_{TIR}$.

9.4. Sensitivity to PAH Size Distribution

As discussed in Section 8, the band strengths are also sensitive to the properties of the PAH population, particularly the size distribution and the fractional ionization $f_{ion}(a)$. Because the peak temperature reached following the absorption of a single UV photon is determined by the heat capacity of the PAH, the emission spectrum depends on the PAH size. Figure 4 shows emission spectra for selected PAH sizes when illuminated by the mMMP ISRF: the emission shifts systematically to longer wavelengths as PAH size increases. In addition, the PAH properties may themselves change systematically with size. Shannon & Boersma (2019) discussed the effect of PAH size on the shape of the 7.7 μm complex.

The sensitivity to the PAH size distribution is explored in Figure 18(a), where filled symbols are for the standard size distribution, open squares are for the PAH size distribution shifted to peak at larger sizes, and open triangles are for the PAH size distribution shifted to smaller sizes. Note that in all cases we hold the lower cutoff fixed at $a_{min} = 4.0$ Å.

The 3.3 μm feature is sensitive to variations in the size distribution, because the 3.3 μm emission is dominated by the smallest PAHs—those with sufficiently small heat capacities such that a single $\sim$10 eV photon can heat the PAH to temperatures $T \gtrsim 600$ K where it can radiate effectively at 3.3 μm. Size distributions shifted to smaller sizes lead to relatively stronger 3.3 μm emission.

In the single-photon heating limit ($U \lesssim 10^3$), larger PAHs are most efficient for converting absorbed starlight energy into emission in the 17 μm feature (see Figure 6), and therefore shifting the PAH size distribution toward larger sizes raises the 17 μm feature strength relative to the other PAH features.

9.5. Sensitivity to PAH Ionization

The sensitivity to the PAH ionization balance is explored in Figure 18(b); filled symbols are for the standard size-dependent ionization fraction $f_{ion}(a)$, while open triangles and squares are for the "high" and "low" ionization fractions, respectively, illustrated in Figure 9. The model postulates that neutral PAHs have enhanced opacity (relative to PAH cations) in the 3.3 μm C–H stretch, and reduced opacity (relative to cations) in the 6.2 μm and 7.7 μm C–C stretching modes. Models with "low" f_{ion} therefore have stronger emission at 3.3 and 11.2 μm, while models with "high" f_{ion} have lower emission in those two bands. Models with high f_{ion} have increased emission in the 6.2 and 7.7 μm bands. Thus, band ratios such as $F(3.3)/F(7.7)$ or $F(11.2)/F(7.7)$ are diagnostic of the environmental conditions determining the PAH ionization balance.

9.6. Sensitivity to Starlight Intensity

At low starlight intensities, the PAH emission is excited by single-photon heating, and the fractional power emitted in each of the bands does not depend on the intensity of the starlight—only on its spectral shape. Figure 19 shows the fractional power $F(\text{band})/F_{TIR}$ in each of the five emission features as a function of U for our standard model, with Figure 19(a) calculated for the quite hard spectrum of a 3 Myr old starburst, and Figure 19(b) calculated for the mMMP spectrum. For the shortest wavelength bands (e.g., 3.3 μm), $F_{clip}(\text{band})/F_{TIR}$ remains relatively constant until U reaches very high values. For longer-wavelength bands, $F_{clip}(\text{band})/F_{TIR}$ begins to rise when some part of the PAH population remains warm enough between photon absorption events to be able to radiate in the band.

As the starlight intensity parameter rises above $U = 1$, the first band affected is the 17 μm complex, with $F_{clip}(17)/F_{TIR}$ initially rising, then dropping as U increases above $\sim$300, and then rising again for $U > 10^{4.5}$. The 17 μm feature is efficiently

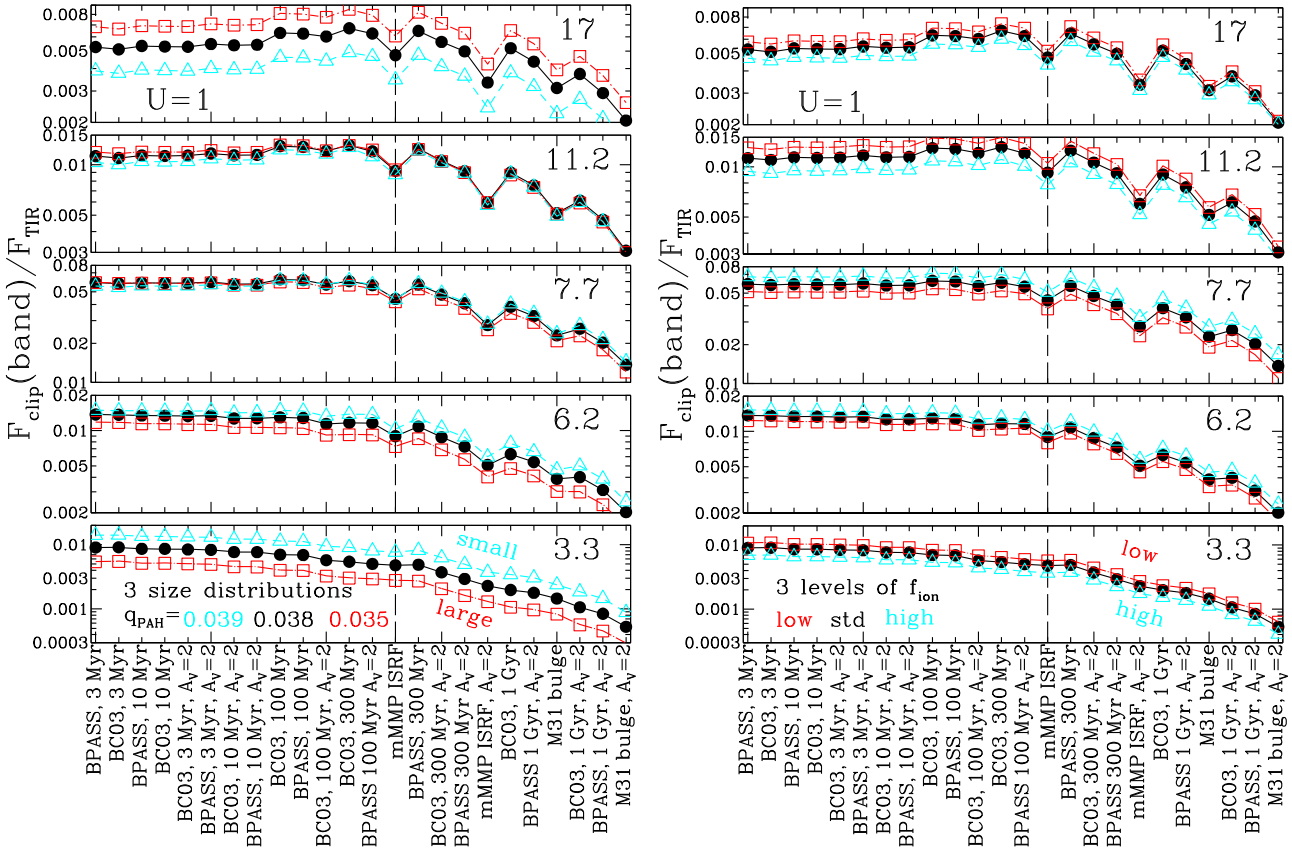

Figure 18. Fractional power $F_{\rm clip}/F_{\rm TIR}$ in selected PAH bands for the dust model heated by different starlight spectra with $U = 1$. (a) Standard ionization and the three size distributions from Figure 9(a). (b) Standard size distribution and the three ionization functions $f_{\rm ion}$ in Figure 9(b).

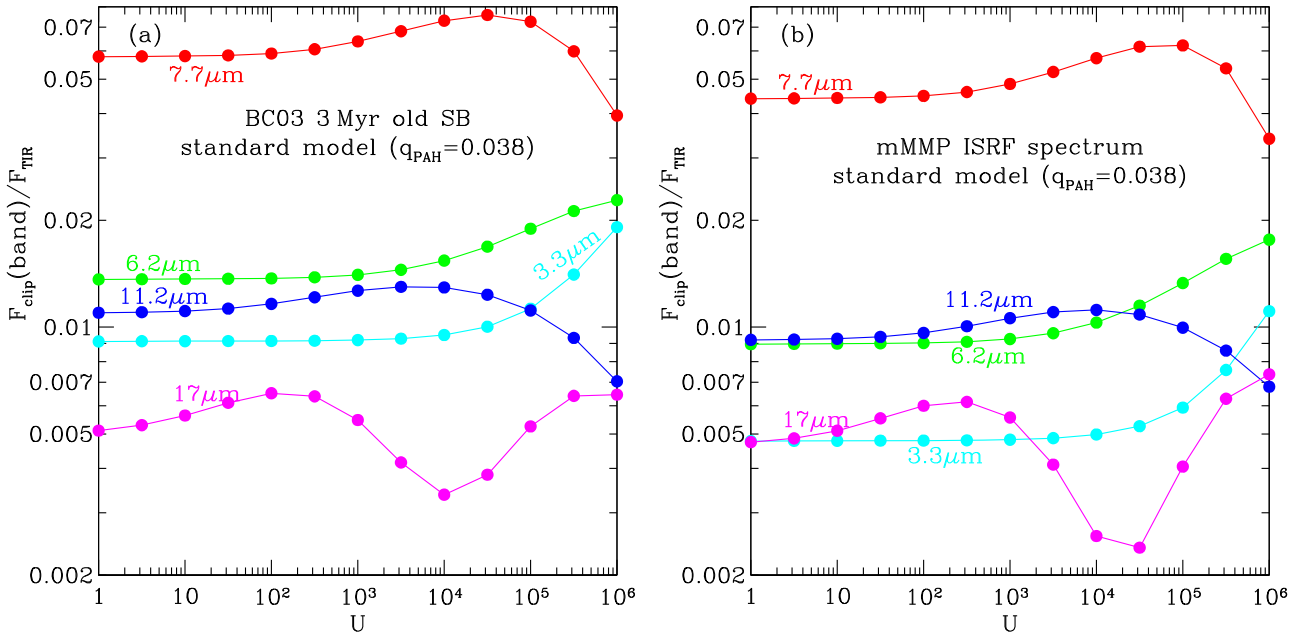

Figure 19. "Clipped" fractional power in selected PAH bands (see Figure 15) for dust model as a function of starlight intensity parameter U, for standard size distribution, standard ionization, and starlight from an (a) 3 Myr old starburst, and (b) mMMP interstellar radiation field.

radiated by PAH nanoparticles with $N_{\rm C} \approx 10^3$–10^4 C atoms (see Figure 6), and for $U \gtrsim 10^2$ these nanoparticles do not fully cool between absorption events. Thermal emission at 17 μm requires temperatures such that $h\nu/kT \lesssim 5$, or $T \gtrsim 170$ K. Figure 20 shows energy distribution functions for PAHs with $N_{\rm C} \approx 1200$ and 5600, for selected values of U. For these two examples, for $U = 10^3$ the nanoparticle spends $\sim$10% of the time above $T > 150$ K, able to radiate in the 17 μm feature. This accounts for the initial rise in $F_{\rm clip}(17)/F_{\rm TIR}$ as U increases to $\sim 10^2$. As U increases beyond $\sim 10^{2.5}$, photons

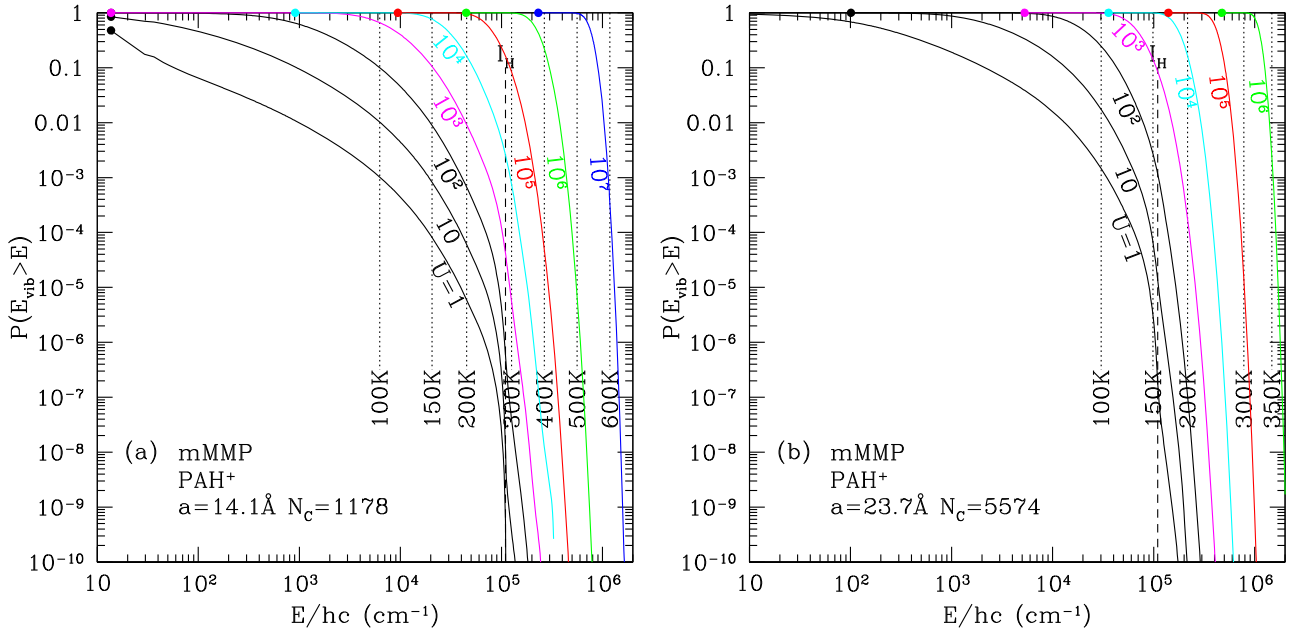

Figure 20. Probability $P(E_{\rm vib} > E)$ of having vibrational energy greater than E, for (a) $a = 14.1$ Å ($N_{\rm C} = 1180$). (b) $a = 23.7$ Å ($N_{\rm C} = 5600$). The vertical dashed line is $I_{\rm H} = 13.6$ eV, the highest photon energy present in the illuminating starlight. For $U = 10^3$, these two nanoparticles spend ~10% of the time at $T > 150$ K, radiating effectively in the 17 μm complex. For $U \geqslant 10^5$, both nanoparticles remain at $T \gtrsim 200$ K, radiating effectively at $\lambda < 15$ μm.

absorbed by an already-warm nanoparticle raise it to higher energies than it would have been able to reach by single-photon heating at lower U. Therefore, energy that for $U \lesssim 10^2$ would be radiated in the 17 μm complex instead is shifted to shorter wavelengths, e.g., the 11.2 μm feature. This explains the drop in $F_{\rm clip}(17)/F_{\rm TIR}$ as U is increased from 10^2 to 10^4.

The decrease in $F_{\rm clip}(17)/F_{\rm TIR}$ to a minimum at $U \approx 10^4$ followed by a rise to a second peak at $U \approx 10^6$ is related to the bimodal size distribution adopted for the PAHs (see Figure 9(a)), with a second component ($a_{02} = 30$ Å) having a mass distribution peaking near $N_C \approx 10^5$. The larger PAHs in this second component account for the second peak in $F_{\rm clip}(17)/F_{\rm TIR}$ at $U \approx 10^6$. For very high U, the larger PAHs are heated to $T \gtrsim 150$ K (see Figure 20) and contribute to the 17 μm feature, accounting for the rise in $F_{\rm clip}(17)/F_{\rm TIR}$ for $U \gtrsim 10^{4.5}$ in Figure 19. For smoother size distributions, the variation of $F_{\rm clip}(17)/F_{\rm TIR}$ would have been reduced. Another complicating factor is that as U reaches $\sim 10^3$, the silicate material in the astrodust grains begins to radiate in the 18 μm silicate feature (see Figure 10(a)). The 18 μm silicate emission profile interferes with the simple method used here for extraction of the flux in the 17 μm feature, which assumes a simple "baseline" between 15.5 and 18.5 μm.

Similar behavior is seen for other bands. $F_{\rm clip}(11.2)/F_{\rm TIR}$ initially rises, and then declines for $U \gtrsim 10^4$ as the PAHs become hot enough to shift power to shorter wavelengths. $F_{\rm clip}(7.7)/F_{\rm TIR}$ rises as U increases to $\sim 10^{4.5}$, followed by a decline as power is shifted to shorter wavelengths. $F_{\rm clip}(6.2)/F_{\rm TIR}$ and $F_{\rm clip}(3.3)/F_{\rm TIR}$ have not yet peaked for the highest intensities $U = 10^6$ considered here.

9.7. Band Ratios

Above we have investigated how PAH band intensities, relative to total infrared (TIR), are affected by the spectrum and intensity of the starlight, and by the PAH size distribution and ionized fraction. Because the band intensities are proportional to the PAH abundance, which can vary, it is useful to see how PAH band *ratios* are affected by the starlight properties, and by the PAH size distribution and ionization. We emphasize that, although trends in ratios among features are conserved, the method employed to recover the feature strengths will affect the median ratio values, sometimes significantly. See Smith et al. (2021, in preparation), for a full suite of comparisons.

Lai et al. (2020) present 2.7–28 μm spectra of galaxies based on Spitzer and AKARI spectroscopy. Their "1C" sample consists of 60 galaxies drawn from the 113 galaxies in their "PAH bright" sample. The 1C sample galaxies were selected to have strong PAH emission but weak silicate features (either in absorption or emission) in order to minimize the effects of reddening. We have applied our simple feature extraction procedure to the Lai et al. (2020) 1C "template" spectrum after subtraction of emission lines from ions and H_2 (T. Lai 2020, private communication). The green diamonds in Figures 21(a)–(d) show the observed band ratios for the Lai et al. (2020) 1C galaxy sample. The error bars shown correspond to the first and ninth deciles for the 1C galaxy sample (T. Lai 2020, private communication).

We have also applied the feature extraction method described in Section 9.1 to 25 galaxies from the Spitzer Infrared Nearby Galaxy Survey (SINGS; Kennicutt et al. 2003; Smith et al. 2007), after removing emission lines (see spectra in Appendix B). Attenuation by dust (though modest) was also corrected for. The band ratios for each galaxy are plotted as triangles in Figures 21(a)–(c). Some of the galaxy points are identified.

Each plot shows a grid for each of three starlight spectra: a 3 Myr old starburst, the mMMP local ISRF, and the M31 bulge stars. The 3 Myr old starburst and M31 bulge spectra span the range from very UV-bright to very red, with the mMMP spectrum falling in between (see Figure 1). The mMMP spectrum is a good estimate for a typical star-forming galaxy.

The model band ratios change when the illuminating stellar spectra are varied, with $F_{\rm clip}(6.2)/F_{\rm clip}(7.7)$ dropping by a

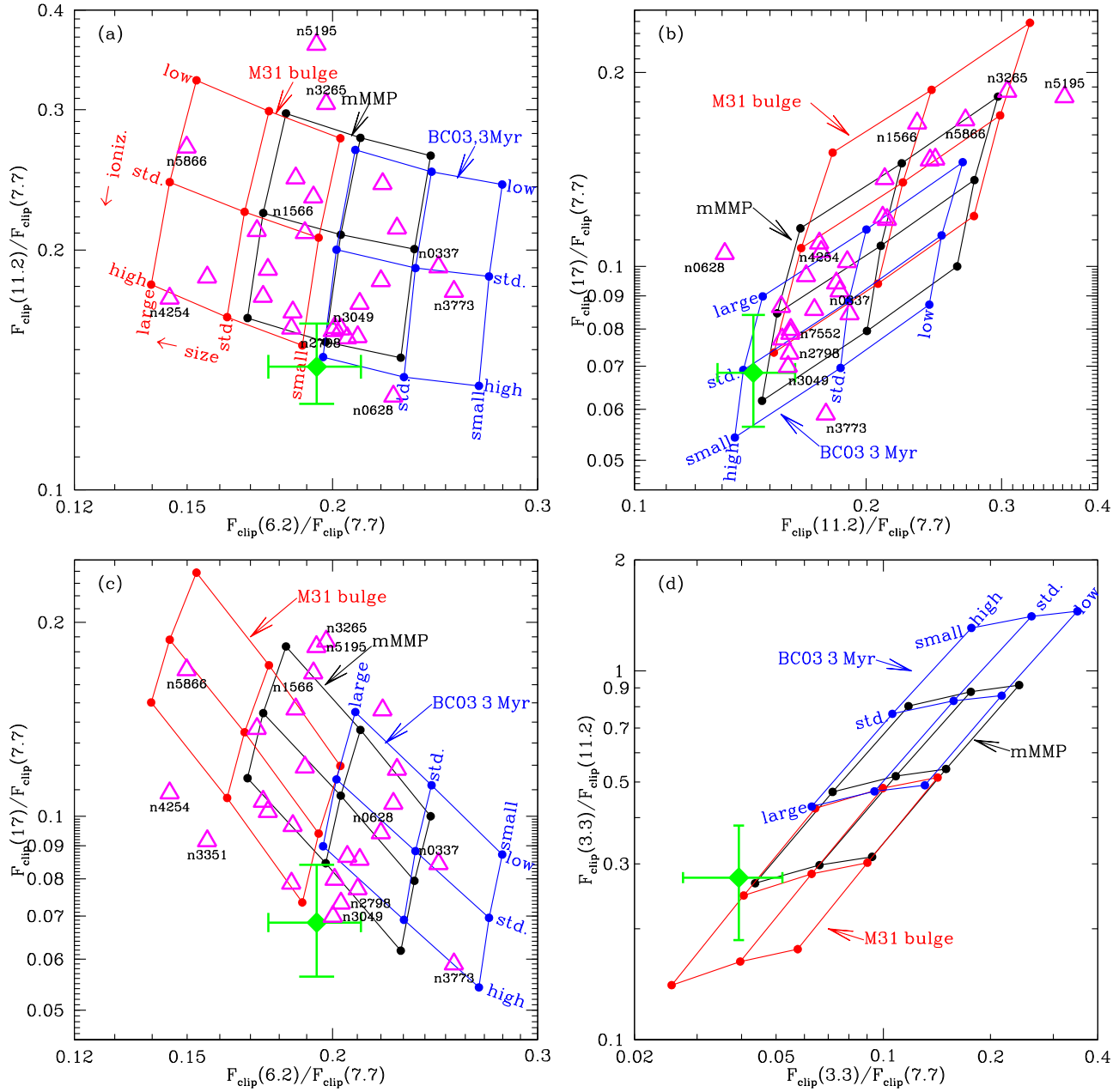

Figure 21. Selected model PAH band ratios calculated for three different starlight spectra (3 Myr old starburst, mMMP radiation field, and M31 bulge spectrum). Band ratios shown are for $U = 1$, but apply for $U \lesssim 10^3$. Results (dots) are shown for three size distributions ("small," "std," and "large"), and three ionization models ("low," "std," and "high"). Triangles show measured ratios for 25 SINGS galaxies (see the text). The green diamond shows band ratios for the 1C galaxy sample of Lai et al. (2020), with error bars showing the first through ninth decile range within the 1C sample.

factor ∼1.5, $F_{\rm clip}(3.3)/F_{\rm clip}(7.7)$ decreasing by a factor ∼2.5, and $F_{\rm clip}(17)/F_{\rm clip}(7.7)$ increasing by a factor ∼2, as the starlight is varied from the 3 Myr starburst to the M31 bulge. Varying the PAH size distributions from "small" to "large" affects the band ratios similarly to changing the spectrum from the 3 Myr starburst to the M31 bulge.

The band ratios for the SINGS galaxies in Figures 21(a)–(c) are generally within the region spanned by the considered variations in PAH size, ionization, and starlight spectra. The "1C" galaxy sample has $F_{\rm clip}(6.2)/F_{\rm clip}(7.7)$ in the middle of the model range, but $F_{\rm clip}(11.2)/F_{\rm clip}(7.7)$ is lower than the models, and lower than 24 of the 25 SINGS galaxies shown. Similarly, the 1C galaxy sample has $F_{\rm clip}(17)/F_{\rm clip}(7.7)$ lower than 24 of the 25 SINGS galaxies shown.

Because the 7.7 μm emission is primarily from PAH cations, $F(11.2)/F(7.7)$ is expected to be sensitive to the PAH ionization, and this is seen in Figures 21(a) and (b). As expected, varying $f_{\rm ion}$ in the model has little effect on $F_{\rm clip}(6.2)/F_{\rm clip}(7.7)$ (the 6.2 μm feature and the 7.7 μm complex are both attributed primarily to cations), but $F_{\rm clip}(11.2)/F_{\rm clip}(7.7)$ decreases by a factor ∼1.5 as $f_{\rm ion}$ varies from the "low" to "high" examples in Figure 9(b). We see in Figures 21(a), (b) that our standard model heated by the mMMP starlight with $U \lesssim 10^4$ gives $F_{\rm clip}(11.2)/F_{\rm clip}(7.7)$ and $F_{\rm clip}(6.2)/F_{\rm clip}(7.7)$ close to observed values for the SINGS galaxies, and the considered variations in size distribution and $f_{\rm ion}$ appear able to accommodate the observed spread in $F_{\rm clip}(6.2)/F_{\rm clip}(7.7)$ and $F_{\rm clip}(11.2)/F_{\rm clip}(7.7)$.

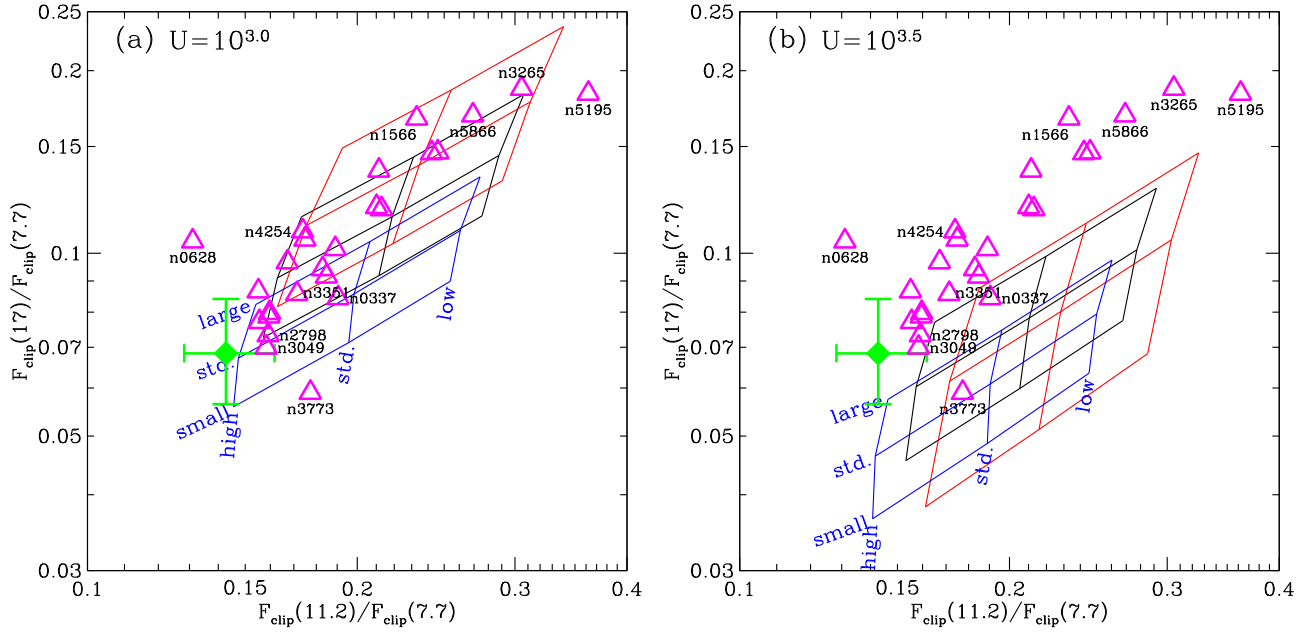

Figure 22. The same as in Figure 21(b), but for $U = 10^3$ and $U = 10^{3.5}$. Note the decrease in the relative strength of the 17 μm feature as U increases beyond 10^3 (see also Figure 19).

Figure 21(c) shows $F_{\rm clip}(17)/F_{\rm clip}(7.7)$ versus $F_{\rm clip}(6.2)/F_{\rm clip}(7.7)$. $F_{\rm clip}(6.2)/F_{\rm clip}(7.7)$ is relatively insensitive to ionization, because both features are thought to be dominated by cations. However, changing the size, or changing the starlight spectrum, does affect $F_{\rm clip}(6.2)/F_{\rm clip}(7.7)$, as already seen in Figure 21(a).

Figure 21(d) shows how $F_{\rm clip}(3.3)/F_{\rm clip}(7.7)$ and $F_{\rm clip}(3.3)/F_{\rm clip}(11.2)$ respond to changes in illuminating spectrum, size distribution, and ionization. Harder spectra (e.g., the 3 Myr starburst) lead to higher values of $F_{\rm clip}(3.3)/F_{\rm clip}(7.7)$ and $F_{\rm clip}(3.3)/F_{\rm clip}(11.2)$ because the larger photon energies lead to higher peak temperatures, enhancing the 3.3 μm emission. Similarly, smaller grains lead to higher $F_{\rm clip}(3.3)/F_{\rm clip}(7.7)$ and $F_{\rm clip}(3.3)/F_{\rm clip}(11.2)$. Thus, $F_{\rm clip}(3.3)/F_{\rm clip}(7.7)$ provides information on size and spectrum, while $F_{\rm clip}(11.2)/F_{\rm clip}(7.7)$ (see Figures 21(a) and (b)) helps constrain $f_{\rm ion}$. We note, however, that our model calculations tend to predict values of $F_{\rm clip}(3.3)/F_{\rm clip}(7.7)$ that are significantly larger than those observed for the 1C sample—this is further discussed in Section 9.9 below. We also see in Figure 21(d) that the 3.3/11.2 band ratio is sensitive to the PAH size distribution, because only the smallest PAHs become hot enough to radiate at 3.3 μm (see Figure 6).

9.8. Modeling the 17μm Emission Feature

Emission features in the 16–19 μm range were reported in a number of Galactic objects by Van Kerckhoven et al. (2000). A characteristic 17 μm complex of features, first identified in NGC 7331 (Smith et al. 2004), is prominent in the emission from star-forming galaxies (Smith et al. 2007). While not yet definitively identified with specific PAH vibrational modes, its correlation with other PAH bands makes it appear likely that the 17 μm feature is also emission from PAHs. Van Kerckhoven et al. (2000) and Boersma et al. (2010) discuss the types of C–C–C bending modes that might be responsible for the 16–19 μm features. The DL07 PAH model used here includes opacity at 17 μm consistent with the observed 17 μm emission from galaxies.

Figure 21(b) shows $F_{\rm clip}(17)/F_{\rm clip}(7.7)$ versus $F_{\rm clip}(11.2)/F_{\rm clip}(7.7)$. The 1C sample average has $F_{\rm clip}(17)/F_{\rm clip}(7.7)$ below the model grids, and lower than all but one of the SINGS galaxies shown. While most of the SINGS galaxies are consistent with our model grids, some have $F_{\rm clip}(17)/F_{\rm clip}(7.7)$ below the model grids in Figure 21(c). The three galaxies with the lowest values of $F_{\rm clip}(17)/F_{\rm clip}(7.7)$ are NGC 2798, NGC 3049, and NGC 3773. Figure 24 shows that each of these galaxies has a continuum that is strongly rising from 20 to 30 μm, indicative of heating by radiation fields with $U \gtrsim 10^3$ (see Figure 10 for model SEDs calculated for $U = 10^3$ and $U = 10^4$). Figure 19 shows that $F_{\rm clip}(17)/F_{\rm TIR}$ is expected to decrease as U is increased from 10^3 to 10^4, suggesting that high U values may explain the low $F_{\rm clip}(17)/F_{\rm clip}(7.7)$ seen for some galaxies.

In Figures 22(a), (b) we show $F_{\rm clip}(17)/F_{\rm clip}(7.7)$ and $F_{\rm clip}(11.2)/F_{\rm clip}(7.7)$ calculated for $U = 10^3$ and $10^{3.5}$. If the heating rate parameter U is increased to $10^{3.0}$ and $10^{3.5}$, $F_{\rm clip}(17)/F_{\rm clip}(7.7)$ is reduced, but $F_{\rm clip}(11.2)/F_{\rm clip}(7.7)$ is hardly affected. This would be one way to lower $F_{\rm clip}(17)/F_{\rm clip}(7.7)$ without changing the PAH properties or size distribution.

Thus, the observed low values of $F_{\rm clip}(17)/F_{\rm clip}(7.7)$ for NGC 2798, NGC 3049, and NGC 3779 might be explained by values of U consistent with the observed 20–30 μm continuum in these galaxies.

9.9. Modeling the 3.3 μm Emission Feature

As already seen in Figure 21(a), the values of $F_{\rm clip}(11.2)/F_{\rm clip}(7.7)$ and $F_{\rm clip}(6.2)/F_{\rm clip}(7.7)$ observed for the SINGS galaxies are in approximate agreement with the model calculations. However, for our standard size distribution ($a_0 = 4$ Å), standard $f_{\rm ion}$, and the mMMP starlight spectrum, the model calculations predict $F_{\rm clip}(3.3\ \mu{\rm m})/F_{\rm clip}(7.7\ \mu{\rm m})$ ratios (see Figure 21(d)), or $F_{\rm clip}(3.3\ \mu{\rm m})/F_{\rm clip}(11.2\ \mu{\rm m})$ ratios

(see Figure 21(c)), that are significantly larger (by about a factor ∼2) than the observed values for the Lai et al. (2020) 1C spectra.

It is possible that the band strengths adopted for the 3.3 μm band are too large. However, the adopted band strengths (from DL07) $\int C_{\rm abs} d\lambda^{-1} = (3.94,\ 0.89) \times 10^{-18}$ cm per C–H bond in (neutral, ionized) PAHs appear to be broadly consistent with results from theoretical calculations (see, e.g., Malloci et al. 2007; Bauschlicher et al. 2018; Yang et al. 2020). With our adopted band strength, the PAH nanoparticles in the model would account for only ∼1/3 of the observed interstellar 3.3 μm absorption feature.[11] If the band strength adopted here is correct, and $f_n \approx 0.5$, most of the observed 3.3 μm absorption must come from aromatic material in larger grains.

For the mMMP spectrum (which we suggest is appropriate for typical star-forming galaxies), the $F_{\rm clip}(3.3)/F_{\rm clip}(7.7)$ ratio could be brought into agreement by shifting to the "large" size distribution ($a_0 = 5$ Å). However, we suspect that the over-prediction of $F_{\rm clip}(3.3\,\mu{\rm m})/F_{\rm clip}(7.7\,\mu{\rm m})$ may be mainly attributable to the neglect of other energy-loss channels: photoelectric emission, photodesorption, and fluorescence (Allamandola et al. 1989). Our calculation of the vibrational excitation of PAHs assumed that absorption of a photon converts the full photon energy $h\nu$ into vibrational excitation, with the vibrational energy then being removed only by infrared emission. However:

1. High-energy photons can photoionize PAHs. When a photoionization takes place, only a fraction of the photon energy appears as "heat."
2. The electronically excited state resulting from absorption of a UV photon may sometimes de-excite by luminescence: emission of an optical photon before "internal conversion" is able to transfer all of the electronic energy to the vibrational modes (see reviews by Witt & Vijh 2004; Witt & Lai 2020).
3. A PAH with a high vibrational temperature may sometimes be able to radiate an optical photon via "Poincare fluorescence" (also known as "recurrent fluorescence"; Leger et al. 1988; Lai et al. 2017).
4. A PAH with a large amount of vibrational energy per degree of freedom will sometimes break a C–H bond, ejecting a hydrogen atom (see, e.g., Marciniak et al. 2021). Neglect of the energy lost to bond-breaking will lead to overestimation of the 3.3 μm emission, which depends on the high-T tail of the temperature distribution function.

PAHs with our "standard" size distribution dn/da and ionization fraction $f_{\rm ion}(a)$, heated by the mMMP starlight spectrum thought to be appropriate for normal star-forming galaxies, may in fact be consistent with observations when the above energy-loss channels are included when calculating the PAH temperature distribution functions and emission. This will be the subject of future work.

[11] If C/H = 37 ppm is in PAHs with H:C::1:3, then the 3.3 μm band strengths adopted here for PAH neutrals and cations (see Table 4 in Appendix A) imply

$$\frac{\int \Delta\tau\, d\lambda^{-1}}{N_{\rm H}} = 4.9(0.23 + 0.77 f_n) \times 10^{-23}\ {\rm cm\ H^{-1}}$$

where $f_n < 1$ is the fraction of the C–H bonds that are in neutral PAHs. The observed absorption toward Cyg OB2-12 in the 3.289 μm aromatic C–H stretch is 7.1×10^{-23} cm H^{-1} (Hensley & Draine 2020).

10. Summary

The principal results of this study are as follows:

1. Using a model that includes a PAH population and a population of larger astrodust grains (Draine & Hensley 2021, B. S. Hensley & B. T. Draine 2021, in preparation) containing amorphous silicates, carbonaceous material, and other compounds, we calculate the infrared emission spectrum for a range of illuminating radiation field spectra, a wide range of starlight intensities, and for the full size distribution of particles in the dust model. We consider starlight spectra ranging from the far-UV-bright spectrum of a 3 Myr old starburst, to the very red spectrum of the highly evolved population of stars in the M31 bulge.
2. We also consider heating of dust in clouds, with the dust inside the cloud irradiated by a reddened (and weakened) radiation field. For the mMMP starlight spectrum, which may be representative of the diffuse radiation in a star-forming galaxy, we find that for fixed PAH abundance, the cloud spectrum has the fractional power in the 3.3 μm feature reduced by a factor ∼1.7. However, the fractional power in the longer-wavelength PAH features, in particular the 7.7 μm complex, is only reduced by a factor ∼1.3.
3. The PAH abundance parameter $q_{\rm PAH}$ can be estimated using the fractional power in the "clipped" 7.7 μm feature: $q_{\rm PAH} = R^{\rm clip}_{q_{\rm PAH}} \times [F_{\rm clip}(7.7\,\mu{\rm m})/F_{\rm TIR}]$. The coefficient $R^{\rm clip}_{q_{\rm PAH}}$ is sensitive to the spectrum of the starlight heating the dust. We estimate $R^{\rm clip}_{q_{\rm PAH}}$ for a variety of starlight spectra and assumptions about the PAH size distribution and ionization.
4. The sensitivity of the PAH emission features to variations in the PAH size distribution is studied. The 3.3 μm feature shows the greatest sensitivity to variations in the PAH size distribution, as these affect the abundance of the smaller PAH nanoparticles that account for most of the 3.3 μm emission. The 3.3 and 11.2 μm features are sensitive to ionization state. The $F_{\rm clip}(6.2\,\mu{\rm m})/F_{\rm clip}(7.7\,\mu{\rm m})$ feature ratio shows a factor of ∼1.5 variations as we vary the PAH size distribution (see Figure 21(a)).
5. The sensitivity of the PAH emission features to the PAH ionization fraction is studied. For changes that correspond to a factor of ∼2 changes in the effective ionization parameter, we find variations by factors ∼1.6 in $F_{\rm clip}(11.2\,\mu{\rm m})/F_{\rm clip}(7.7\,\mu{\rm m})$ (see Figures 21(a) and (b)).
6. The 17 μm feature strength is sensitive to the intensity of the starlight heating the dust. The relatively low values of $F_{\rm clip}(17)/F_{\rm clip}(7.7)$ observed in some SINGS galaxies and in the 1C galaxy sample of Lai et al. (2020) may be explained by high values of the heating rate parameter $U \approx 10^3$.
7. The treatment of PAH excitation by starlight used here has neglected several energy-loss channels, resulting in overestimation of the 3.3 μm emission for a given PAH size distribution, as discussed in Section 9.9.
8. A library of dust and PAH emission spectra for a wide range of starlight spectra and starlight intensities is available online (https://doi.org/10.7910/DVN/LPUHIQ). A companion paper (Smith et al. 2021, in preparation) will use this library to interpret observed spectra using the PAHFIT spectral-fitting code.

This research was supported in part by NSF grants AST-1408723 and AST-1908123, and NASA grant NSSC19K0572. We especially thank Thomas Lai for making available the observed galaxy spectra in advance of publication, and for providing a line-subtracted average 1C spectrum. Finally, we thank the anonymous referee for a detailed and expert report that helped us improve the manuscript.

Appendix A
PAH Absorption Cross Sections

In this work we follow the recommendations of DL07 to estimate photon absorption cross sections for PAHs. For a PAH with $N_{\rm C}$ carbon atoms, we take a weighted average of $N_{\rm C}\Gamma(\lambda)$, where $\Gamma(\lambda)$ is an estimate for "pure PAH" absorption per C atom, and $C_{\rm abs}^{\rm (gra)}(\lambda)$, the absorption cross section for a graphite sphere:

$$C_{\rm abs}(\lambda) = \xi_{\rm PAH} N_C \Gamma(\lambda) + (1 - \xi_{\rm PAH}) C_{\rm abs}^{\rm (gra)}(\lambda). \quad \text{(A1)}$$

The ad hoc weighting factor $\xi_{\rm PAH}$ varies between 0.99 and 0 with increasing N_C:

$$\xi_{\rm PAH} = 0.99 \times \min\left[1, \frac{5\times 10^4}{N_C}\right]. \quad \text{(A2)}$$

We use $C_{\rm abs}^{\rm (gra)}$ estimated for turbostratic graphite by Draine (2016), using Maxwell–Garnet effective medium theory with $\epsilon(\mathbf{E}\|c)$ for the matrix and $\epsilon(\mathbf{E}\perp c)$ for inclusions. The "pure PAH" contribution to the cross section per C is given by

$$\Gamma(\lambda) = S_1(\lambda) + (1.35x - 3)\times 10^{-18}\,{\rm cm}^2 \quad \text{for } 10 < x < 15 \quad \text{(A3)}$$

$$= (66.302 - 24.367x + 2.950x^2 - 0.1057x^3)\times 10^{-18}\,{\rm cm}^2 \quad \text{for } 7.7 < x < 10 \quad \text{(A4)}$$

$$= S_2(\lambda) + c_0 + c_1 x + c_2(x-5.9)^2 + c_3(x-5.9)^3 \quad \text{for } 5.9 < x < 7.7 \quad \text{(A5)}$$

$$= S_2(\lambda) + c_0 + c_1 x \quad \text{for } 3.3 < x < 5.9 \quad \text{(A6)}$$

$$= 34.58\times 10^{-18-3.431/x}\,{\rm cm}^2 C(\lambda/\lambda_c) + \sum_{j=3}^{30} S_j(\lambda) \quad \text{for } x < 3.3 \quad \text{(A7)}$$

where

$$x \equiv \mu{\rm m}/\lambda \quad \text{(A8)}$$

$$c_0 = 1.8687\times 10^{-18}\,{\rm cm}^2 \quad \text{(A9)}$$

$$c_1 = 1.905\times 10^{-19}\,{\rm cm}^2 \quad \text{(A10)}$$

$$c_3 = 4.175\times 10^{-19}\,{\rm cm}^2 \quad \text{(A11)}$$

$$c_4 = 4.37\times 10^{-20}\,{\rm cm}^2 \quad \text{(A12)}$$

$$S_j(\lambda) \equiv \frac{2}{\pi}\sum \frac{\gamma_j \lambda_j \sigma_{{\rm int},j}}{(\lambda/\lambda_j - \lambda_j/\lambda)^2 + \gamma_j^2} \quad \text{(A13)}$$

and

$$C(y) \equiv \frac{1}{\pi}\arctan\left[\frac{10^3(y-1)^3}{y}\right] + \frac{1}{2} \quad \text{(A14)}$$

is the cutoff function proposed by Desert et al. (1990). The wavelength λ_c for the onset of PAH electronic absorption is taken to be (see the discussion in Salama et al. 1996)

$$\lambda_c = \frac{0.951\ \mu{\rm m}}{1 + 3.616/\sqrt{M}} \quad \text{for neutral PAHs,} \quad \text{(A15)}$$

$$= \frac{1.125\ \mu{\rm m}}{1 + 2.567/\sqrt{M}} \quad \text{for PAH cations,} \quad \text{(A16)}$$

where the number of rings M is taken to be

$$M = 0.3N_{\rm C} \quad \text{for } N_{\rm C} \leqslant 40 \quad \text{(A17)}$$

$$= 0.4N_{\rm C} \quad \text{for } N_{\rm C} > 40. \quad \text{(A18)}$$

The central wavelength λ_j, fractional width γ_j, and integrated absorption σ_j for the Drude profiles are given in Table 4. Most of the adopted parameters are unchanged from DL07. However, the strength of the feature at 14.19 μm ($j = 23$) and the strength of the 17 μm complex ($j = 26$, 27, 28) have been increased by 33% to improve agreement with observed spectra.

Figure 23 shows the absorption cross sections (per C atom) used to model PAH neutrals and cations, for the specific example of PAHs with $N_{\rm C} = 90$ C atoms.

Table 4
PAH Resonance Parameters[a]

j	λ_j (μm)	γ_j	$\sigma_{\mathrm{abs}j} \equiv \int \sigma_{\mathrm{abs},j} d\lambda^{-1}$ Neutral (10^{-20} cm/C)	Ionized (10^{-20} cm/C)	Tentative Identification	Note
1	0.0722	0.195	7.97×10^7	7.97×10^7	$\sigma \rightarrow \sigma^*$ transition in aromatic C	[b]
2	0.2175	0.217	1.23×10^7	1.23×10^7	$\pi \rightarrow \pi^*$ transition in aromatic C	[b]
3	1.050	0.055	0	2.0×10^4	Weak electronic transition in PAH cation	[c]
4	1.260	0.11	0	7.8×10^3	Weak electronic transition in PAH cation	[c]
5	1.905	0.09	0	−146.5	?	[c]
6	3.300	0.012	394(H/C)	89.4(H/C)	Aromatic C–H stretch	[d]
7	5.270	0.034	2.5	20	C–H bend + C–H stretch combination mode	
8	5.700	0.035	4	32	C–H and + C–H stretch combination mode	
9	6.220	0.030	29.4	235	Aromatic C–C stretch (in-plane)	
10	6.690	0.070	7.35	59	?	
11	7.417	0.126	20.8	181	Aromatic C–C stretch	
12	7.598	0.044	18.1	163	Aromatic C–C stretch	
13	7.850	0.053	21.9	197	C–C stretch + C–H bending	
14	8.330	0.052	6.94(H/C)	48.4(H/C)	C–C stretch + C–H bending?	
15	8.610	0.039	27.8(H/C)	194(H/C)	C–H in-plane bending	
16	10.68	0.020	0.3(H/C)	0.3(H/C)	C–H out-of-plane bending, solo?	
17	11.23	0.012	18.9(H/C)	17.7(H/C)	C–H out-of-plane bending, solo	
18	11.33	0.032	52(H/C)	49(H/C)	C–H out-of-plane bending, solo	
19	11.99	0.045	24.2(H/C)	20.5(H/C)	C–H out-of-plane bending, duo	
20	12.62	0.042	34.8(H/C)	31.0(H/C)	C–H out-of-plane bending, trio	
21	12.69	0.013	1.3(H/C)	1.3(H/C)	C–H out-of-plane bending, trio	
22	13.48	0.040	8.0(H/C)	8.0(H/C)	C–H out-of-plane bending, quartet?	
23	14.19	0.025	0.60	0.60	C–H out-of-plane bending, quartet?	[e]
24	15.90	0.020	0.04	0.04	?	
25	16.447	0.014	0.5	0.5	C–C–C bending?	
26	17.04	0.065	2.99	2.99	C–C–C bending?	[e]
27	17.375	0.012	0.15	0.15	C–C–C bending?	[e]
28	17.87	0.016	0.090	0.090	C–C–C bending?	[e]
29	18.92	0.10	0.10	0.17	C–C–C bending?	
30	15.	0.8	50.0	50.0	large-scale bending modes	

Notes.
[a] Values taken from DL07 except as noted.
[b] Li & Draine (2001).
[c] Draine & Li (2007).
[d] Mattioda et al. (2005a, 2005b).
[e] Increased by 33% from DL07.

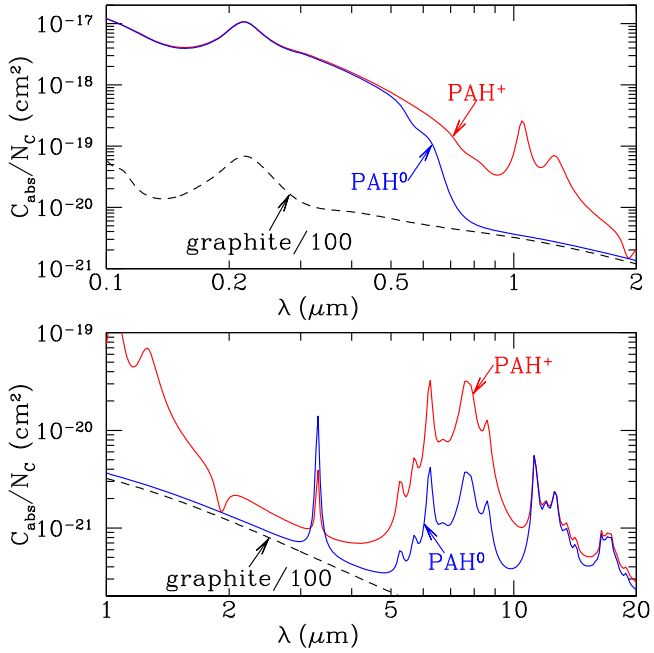

Figure 23. Model absorption cross section per C atom for $a = 0.0006$ μm PAH^0 and PAH$^+$ with $N_C = 90$ C atoms. Also shown is 1% of the cross section per C for turbostratic graphite.

Appendix B
Sample Spectra

Spectra for 25 of the SINGS galaxies (Smith et al. 2007), after removal of emission lines and approximate subtraction of starlight, are shown in Figure 24. For four galaxies[12], the observed spectra showed evidence of extinction in the silicate feature; the spectra used here have been corrected for extinction. For each spectrum, the "clip lines" are shown in red.

[12] NGC 1482, NGC 4536, NGC 5866, NGC 6946.

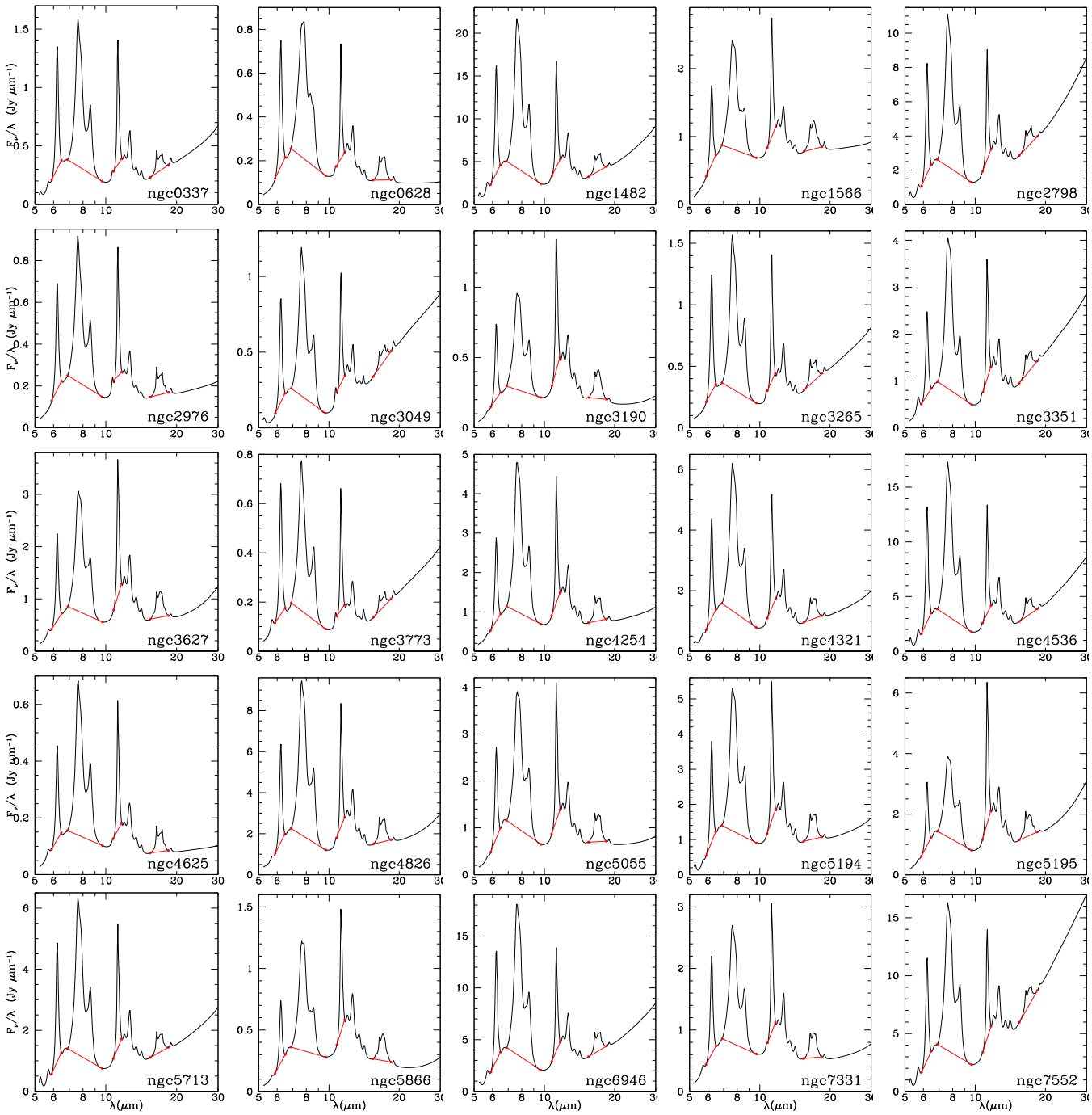

Figure 24. Line-subtracted and attenuation-corrected spectra of 25 SINGS galaxies (Smith et al. 2007), showing clip lines used for extracting $F_{\rm clip}$.

ORCID iDs

B. T. Draine https://orcid.org/0000-0002-0846-936X
Aigen Li https://orcid.org/0000-0002-1119-642X
Brandon S. Hensley https://orcid.org/0000-0001-7449-4638
L. K. Hunt https://orcid.org/0000-0001-9162-2371
K. Sandstrom https://orcid.org/0000-0002-4378-8534
J.-D. T. Smith https://orcid.org/0000-0003-1545-5078

References

Allamandola, L. J., Hudgins, D. M., & Sandford, S. A. 1999, ApJL, 511, L115
Allamandola, L. J., Tielens, A. G. G. M., & Barker, J. R. 1985, ApJL, 290, L25
Allamandola, L. J., Tielens, A. G. G. M., & Barker, J. R. 1989, ApJS, 71, 733
Armus, L., Charmandaris, V., & Soifer, B. T. 2020, NatAs, 4, 467
Bauschlicher, C. W. J., Boersma, C., Ricca, A., et al. 2010, ApJS, 189, 341
Bauschlicher, C. W. J., Ricca, A., Boersma, C., & Allamandola, L. J. 2018, ApJS, 234, 32
Boersma, C., Bauschlicher, C. W., Allamandola, L. J., et al. 2010, A&A, 511, A32
Boersma, C., Bauschlicher, C. W. J., Ricca, A., et al. 2014, ApJS, 211, 8
Bohlin, R. C., Savage, B. D., & Drake, J. F. 1978, ApJ, 224, 132
Brandl, B. R., Bernard-Salas, J., Spoon, H. W. W., et al. 2006, ApJ, 653, 1129
Bruzual, G., & Charlot, S. 2003, MNRAS, 344, 1000
DeFrees, D. J., Miller, M. D., Talbi, D., Pauzat, F., & Ellinger, Y. 1993, ApJ, 408, 530
Desert, F.-X., Boulanger, F., & Puget, J. L. 1990, A&A, 237, 215
Draine, B. T. 2003, ARA&A, 41, 241
Draine, B. T. 2011a, in EAS Publications Ser. 46, PAHs and the Universe, ed. C. Joblin & A. G. G. M. Tielens (Les Ulis: EDP Sciences), 29

Draine, B. T. 2011b, Physics of the Interstellar and Intergalactic Medium (Princeton, NJ: Princeton Univ. Press)
Draine, B. T. 2016, ApJ, 831, 109
Draine, B. T., & Anderson, N. 1985, ApJ, 292, 494
Draine, B. T., Aniano, G., Krause, O., et al. 2014, ApJ, 780, 172
Draine, B. T., & Hensley, B. S. 2021, ApJ, 909, 94
Draine, B. T., & Li, A. 2001, ApJ, 551, 807
Draine, B. T., & Li, A. 2007, ApJ, 657, 810
Eldridge, J. J., Stanway, E. R., Xiao, L., et al. 2017, PASA, 34, e058
Fazio, G. G., Hora, J. L., Allen, L. E., et al. 2004, ApJS, 154, 10
Fink, J., Müller-Heinzerling, T., Pflüger, J., et al. 1983, SSCom, 47, 687
Fitzpatrick, E. L., Massa, D., Gordon, K. D., Bohlin, R., & Clayton, G. C. 2019, ApJ, 886, 108
Galliano, F., Madden, S. C., Tielens, A. G. G. M., Peeters, E., & Jones, A. P. 2008, ApJ, 679, 310
Groves, B., Krause, O., Sandstrom, K., et al. 2012, MNRAS, 426, 892
Guhathakurta, P., & Draine, B. T. 1989, ApJ, 345, 230
Helou, G., Roussel, H., Appleton, P., et al. 2004, ApJS, 154, 253
Hemachandra, D., Barmby, P., Peeters, E., et al. 2015, MNRAS, 454, 818
Hensley, B. S., & Draine, B. T. 2020, ApJ, 895, 38
Hensley, B. S., & Draine, B. T. 2021, ApJ, 906, 73
Kennicutt, R. C., Armus, L., Bendo, G., et al. 2003, PASP, 115, 928
Kim, S.-H., Martin, P. G., & Hendry, P. D. 1994, ApJ, 422, 164
Lai, T. S. Y., Smith, J. D. T., Baba, S., Spoon, H. W. W., & Imanishi, M. 2020, ApJ, 905, 55
Lai, T. S. Y., Witt, A. N., & Crawford, K. 2017, MNRAS, 469, 4933
Leger, A., Boissel, P., & d'Hendecourt, L. 1988, PhRvL, 60, 921
Leger, A., & Puget, J. L. 1984, A&A, 137, L5
Lenz, D., Hensley, B. S., & Doré, O. 2017, ApJ, 846, 38
Li, A. 2020, NatAs, 4, 339
Li, A., & Draine, B. T. 2001, ApJ, 554, 778
Li, A., & Draine, B. T. 2002, ApJ, 572, 232
Lu, N., Helou, G., Werner, M. W., et al. 2003, ApJ, 588, 199
Malloci, G., Joblin, C., & Mulas, G. 2007, CP, 332, 353
Maragkoudakis, A., Peeters, E., & Ricca, A. 2020, MNRAS, 494, 642
Marciniak, A., Joblin, C., Mulas, G., Rao Mundlapati, V., & Bonnamy, A. 2021, arXiv:2103.03890
Mathis, J. S., Mezger, P. G., & Panagia, N. 1983, A&A, 128, 212
Matsuura, M., Bernard-Salas, J., Lloyd Evans, T., et al. 2014, MNRAS, 439, 1472
Mattioda, A. L., Allamandola, L. J., & Hudgins, D. M. 2005a, ApJ, 629, 1183
Mattioda, A. L., Hudgins, D. M., & Allamandola, L. J. 2005b, ApJ, 629, 1188
Mori, T. I., Sakon, I., Onaka, T., et al. 2012, ApJ, 744, 68
Peeters, E., Hony, S., Van Kerckhoven, C., et al. 2002, A&A, 390, 1089
Ricca, A., Bauschlicher, C. W. J., Boersma, C., Tielens, A. G. G. M., & Allamandola, L. J. 2012, ApJ, 754, 75
Riechers, D. A., Pope, A., Daddi, E., et al. 2014, ApJ, 786, 31
Salama, F., Bakes, E. L. O., Allamandola, L. J., & Tielens, A. G. G. M. 1996, ApJ, 458, 621
Schlafly, E. F., Meisner, A. M., Stutz, A. M., et al. 2016, ApJ, 821, 78
Schutte, W. A., Tielens, A. G. G. M., & Allamandola, L. J. 1993, ApJ, 415, 397
Sellgren, K., Werner, M. W., & Dinerstein, H. L. 1983, ApJL, 271, L13
Shannon, M. J., & Boersma, C. 2019, ApJ, 871, 124
Siebenmorgen, R., Voshchinnikov, N. V., & Bagnulo, S. 2014, A&A, 561, A82
Smith, J. D. T., Dale, D. A., Armus, L., et al. 2004, ApJS, 154, 199
Smith, J. D. T., Draine, B. T., Dale, D. A., et al. 2007, ApJ, 656, 770
Stanway, E. R., & Eldridge, J. J. 2018, MNRAS, 479, 75
Tielens, A. G. G. M. 2008, ARA&A, 46, 289
Van Kerckhoven, C., Hony, S., Peeters, E., et al. 2000, A&A, 357, 1013
Weingartner, J. C., & Draine, B. T. 2001, ApJ, 548, 296
Witt, A. N., & Lai, T. S. Y. 2020, Ap&SS, 365, 58
Witt, A. N., & Vijh, U. P. 2004, in ASP Conf. Ser. 309, Astrophysics of Dust, ed. A. N Witt, G. C. Clayton, & B. T. Draine (San Francisco, CA: ASP), 115
Xie, Y., Ho, L. C., Li, A., & Shangguan, J. 2018, ApJ, 867, 91
Yang, X. J., Li, A., & Glaser, R. 2020, ApJS, 251, 12